International Journal of
Molecular Sciences

MDPI

Article

Structure–Reactivity Relationships in *N*-Methylpyridinium Aldoxime Isomers: Comparative Experimental and Computational Studies

Danijela Musija [1], Igor Picek [1], Robert Vianello [2], Dubravka Matković-Čalogović [3], Blaženka Foretić [1] and Vladimir Damjanović [1,*]

[1] Department of Chemistry and Biochemistry, School of Medicine, University of Zagreb, 10000 Zagreb, Croatia; danijela.musija@mef.hr (D.M.); igor.picek@mef.hr (I.P.); blazenka.foretic@mef.hr (B.F.)
[2] Laboratory for the Computational Design and Synthesis of Functional Materials, Division of Organic Chemistry and Biochemistry, Ruđer Bošković Institute, 10000 Zagreb, Croatia; robert.vianello@irb.hr
[3] Department of Chemistry, Faculty of Science, University of Zagreb, 10000 Zagreb, Croatia; dubravka@chem.pmf.hr
* Correspondence: vladimir.damjanovic@mef.hr

Abstract

The relative position of the oxime group within pharmaceutically relevant pyridinium oximes is a pivotal factor that governs their intrinsic physicochemical properties and their biological reactivity. However, studies providing in-depth, molecular-level insight into these structure–reactivity relationships are still limited. In this work, we present an integrated experimental and computational study of *N*-methylpyridinium-2-aldoxime chloride (PAM2-Cl), *N*-methylpyridinium-3-aldoxime iodide (PAM3-I), and *N*-methylpyridinium-4-aldoxime iodide (PAM4-I), aimed at elucidating discrete differences in their ionization behavior, electronic structure, σ-donor properties, and nucleophilicity. The crystal structure of PAM3-I was determined by X-ray diffraction. Comparative structural and spectroscopic (UV–Vis, NMR, IR) analyses elucidated the structural and electronic effects arising from the position of the oxime group. Kinetic studies of substitution reactions with aquapentacyanoferrate(II) in aqueous solution enabled the determination of pentacyano(PAM)ferrate(II) formation and dissociation rate constants, coordination modes, pK_a values of the coordinated ligands, complex stability constants, and σ-donating capabilities. The DFT-based analysis of atomic charge distribution transcended experimental limitations, offering a new perspective on electronic structure-related properties. This study presents the first side-by-side, internally consistent structure–reactivity map across PAM2, PAM3, and PAM4 isomers that triangulates crystallography, UV–Vis-derived pK_a values, substitution kinetics, and DFT descriptors in a single framework.

Keywords: *N*-methylpyridinium aldoximes; pentacyanoferrates(II); spectroscopy; kinetics; DFT calculations

Academic Editor: Michał Zabiszak

Received: 30 January 2026
Revised: 15 February 2026
Accepted: 17 February 2026
Published: 20 February 2026

1. Introduction

Pyridinium oximes have sustained research interest for over six decades, primarily due to their high potency as antidotes against highly toxic organophosphorus (OP) compounds [1]. OP compounds—widely used as pesticides and historically developed as

nerve agents—exert acute neurotoxicity by phosphorylating the serine hydroxyl group within the acetylcholinesterase (AChE) active site. This process produces an inactive OP–AChE adduct, leading to the excessive accumulation of acetylcholine at cholinergic synapses and a life-threatening cholinergic crisis [2]. The pharmacological application of pyridinium oximes arises from their ability to displace the phosphoryl moiety and reactivate the enzyme. This mode of action is rooted in the chemical nature of the oxime group (>C=NOH); its acidic character facilitates deprotonation to the oximate ion (>C=NO$^-$) under physiological conditions, which acts as a powerful α-nucleophile with pronounced esterolytic capability. This property enables oximes to esterolytically reactivate OP-inhibited AChE [1], exert thioesterolytic activity [3–5], or act as catalysts that mimic the catalytic mode of AChE [6]. When an oxime group is directly attached to a pyridinium system, a key structural motif is established that allows for precise supramolecular docking within the inactive OP–AChE, followed by the efficient nucleophilic cleavage of the phosphoester bond and subsequent restoration of enzyme activity [7]. Furthermore, pyridinium oximes can bind to the active and/or allosteric sites of native AChE as reversible inhibitors, thereby indirectly protecting the enzyme from irreversible inhibition [8].

Early research on oxime reactivators predominantly focused on in vitro reactivation kinetics, enzyme–reactivator binding interactions, and clinical effectiveness against various OP insecticides and nerve agents [9–11]. These studies identified key physicochemical parameters governing reactivation potency: the pK_a of the oxime group, which dictates the concentration of the nucleophilically active oximate anion, and the nature of the *N*-substituent, critical for blood–brain barrier (BBB) penetration. These properties are further modulated by electronic and steric effects, including the number of pyridinium rings and oxime groups, the position of oxime groups on the pyridinium rings, the length and structural features of the linker connecting pyridinium rings, and the presence of non-oxime substituents on the pyridinium rings [8,12]. Furthermore, investigations on the reactivation efficacy of *N*-methylpyridinium oxime positional isomers—including pralidoxime (PAM2), PAM3, and PAM4—revealed that the type and chemical nature of the OP compound are equally important factors determining antidotal efficacy. Specifically, PAM2 is more effective in reactivating leptophos-oxon-inhibited AChE than PAM4, whereas the most potent reactivators against chlorpyrifos inhibition are 4-substituted pyridinium oximes [12,13]. Extensive investigations of mono- and bis-pyridinium oximes conducted from the 1950s to the 1990s ultimately resulted in the clinical use of pralidoxime, obidoxime (LüH-6), trimedoxime (TMB-4), and asoxime (HI-6). These compounds remain the only clinically deployed oximes due to the regulatory approval and well-established therapeutic protocols [14]. Despite decades of use, however, these oximes exhibit significant limitations, including an insufficiently broad spectrum of action, limited bioavailability and poor BBB passage, inadequate stability, toxicity, poor selectivity for AChE, and insufficient reactivation rates [15].

To overcome these limitations, current research on pyridinium oxime antidotes has shifted toward complementary and multidisciplinary approaches. Theoretical and computational studies now provide detailed structural insights, enabling the rational design of compounds through molecular docking, molecular dynamics, and structure–activity relationship (SAR) analyses [16–18]. These efforts are bolstered by crystallographic structures of native and OP-inhibited AChE, as well as "aged" OP–AChE conjugates [19,20]. Notable advancements include K-oximes, which show improved reactivation of tabun-inhibited AChE and reduced toxicity compared with obidoxime in vivo [21]; nonquaternary oximes that are emerging as efficient reactivators of OP-inhibited butyrylcholinesterase—a supporting enzyme and biological scavenger of OP compounds [22]; and nanopyridinium oxime transport systems designed to enhance BBB crossing [23].

Despite extensive research on pyridinium oximes, systematic and comparative investigations of their intrinsic molecular properties that correlate X-ray crystallographic, spectroscopic, and physicochemical data remain limited, particularly for positional pyridinium oxime isomers. This rationalizes the need for establishing a comparative and internally consistent structure–reactivity map across these classical pyridinium oximes by integrating crystallographic data, spectroscopic analyses, ligand substitution kinetics, and density functional theory (DFT) descriptors within a single framework.

Although the crystal structures of PAM2 halides were solved in 1966 [24], PAM4-I and PAM4-Cl·H_2O were structurally characterized only in 2013 by our group [25], and the structure of PAM3 remained unknown. Theoretical studies incorporating DFT-based quantum-chemical calculations have been sporadic and have primarily focused on the stability of different geometrical and conformational forms of pyridinium oximes [26,27]. Experimental comparative studies have mainly addressed various *N*-substituted mono- and bis-pyridinium-4-oximes, revealing interdependence between crystal and electronic structure, ionization properties, reactivity, and stability in aqueous media for alkyl, benzyl and carbonyl derivatives [25,28]. In addition, σ-donating and π-accepting properties of pyridinium-4-oxime derivatives, together with their coordination ability, were established using the aquapentacyanoferrate(II) model complex $[Fe^{II}(CN)_5(H_2O)]^{3-}$ [25,29]. Although pentacyano(ligand)ferrate(II) complexes are currently being explored as iron-based photosensitizers [30], drug-delivery systems [31], metal-mediated oxidative prodrug activators [32], and highly sensitive solvatochromic probes [33], the $[Fe^{II}(CN)_5(H_2O)]^{3-}$ ion has long been recognized as a well-established model system for studying ligand substitution reactions. Its well-defined coordination environment, comprising five inert cyanide ligands and a single labile aqua ligand, enables systematic evaluation of ligand reactivity, Lewis basicity, and electronic properties. Kinetic studies involving aromatic nitrogen heterocycles and other nitrogen- and sulfur-donor ligands have revealed a direct correlation between ligand electron-donating ability (basicity) and electronic properties with both substitution rate constants and complex stability constants. These studies highlight the pronounced sensitivity of the $[Fe(CN)_5(H_2O)]^{3-}$ complex to the electronic and steric characteristics of incoming ligands [34,35].

Most recently, mono- and bis-pyridinium-4-oxime derivatives have been recognized as electron-accepting building blocks that exhibit pronounced hydrogen-bonding propensity, functioning both as H-bond donors and H-bond acceptors, and their stimuli-responsive hydrochromic supramolecular hexacyanoferrate(II) complexes have been reported [36,37].

In this study, we employ an integrated experimental and theoretical approach to investigate *N*-methylpyridinium-2-aldoxime chloride (PAM2-Cl), *N*-methylpyridinium-3-aldoxime iodide (PAM3-I), and *N*-methylpyridinium-4-aldoxime iodide (PAM4-I), along with their pentacyano(PAM)ferrate(II) complexes, in order to establish a coherent molecular-level framework for understanding how positional isomerism governs the physicochemical and coordination properties of pyridinium oximes in aqueous solution. The crystal structure of PAM3-I is determined and reported here for the first time. Through comparative structural and spectroscopic analyses, combined with kinetic studies of pentacyano(PAM)ferrate(II) complex formation and dissociation, and supported by complementary DFT calculations, we provide detailed insights into the subtle differences in nucleophilicity, structural, electronic, acid–base, and coordination properties among these positional isomers.

https://doi.org/10.3390/ijms27042015

2. Results and Discussion

2.1. N-Methylpyridinium Aldoximes

2.1.1. The Crystal and Molecular Structure of PAM3-I

PAM3-I crystallizes in the orthorhombic crystal system, space group *P*bca (Table S1). The asymmetric unit contains an *N*-methylpyridinium-3-aldoxime cation and an iodide ion. The molecular structure is shown in Figure 1. The bond lengths and angles given in Table S2 indicate electron delocalization within the pyridinium ring. The oxime C1=N1 bond of 1.259(3) Å is a typical double bond. The oxime substituent has an *E* configuration. The two planar moieties, *N*-methylpyridinium and oxime, are inclined by an angle of 14.66°. This is contrary to the *N*-methylpyridinium-2-aldoxime cation in the crystal structure of PAM2-Cl [38], and *N*-methylpyridinium-4-aldoxime cations in PAM4-I and PAM4-Cl·H_2O [25] where the cations are planar. Packing in the crystal structure is dominated by a hydrogen bond of 3.543(2) Å that links the cation oxime hydroxyl group and the iodide anion, O1–H···I (Table S3), while the other contacts are only weak van der Waals interactions (Figure S1).

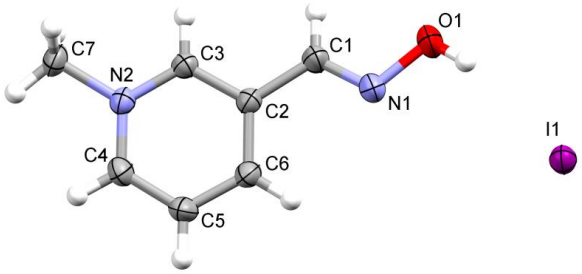

Figure 1. Molecular structure of PAM3-I.

2.1.2. Spectral and Ionization Properties

The UV–Vis spectra of the *N*-methylpyridinium aldoxime ligands, recorded in buffered aqueous solutions over a pH range 4–11.5 (Figures 2, S2 and S3; spectral data in Table S4), are characterized by two dominant and clearly pH-dependent absorption bands. These bands can be unambiguously assigned to π→π* electronic transitions associated with the protonated ($PAMH^+$) and deprotonated (PAM^0) forms of the aldoxime ligands, respectively (Table S4). Systematic spectral changes observed upon variation in pH reflect the acid–base equilibrium between these two species and provide direct spectroscopic evidence for aldoxime deprotonation, aligning with previously reported data [39,40]. The acid ionization constants were determined from pH-dependent changes in absorbance monitored at the respective absorption maxima of the protonated and deprotonated forms (Figure S4, Table S4). The pK_a values obtained in this work for PAM2-Cl (7.97 ± 0.04) and PAM3-I (9.42 ± 0.03) at 25.0 °C and ionic strength I = 0.10 mol dm^{-3}, along with the value for PAM4-I (8.56 ± 0.05) previously determined under matched conditions using an identical methodology [25], are in excellent agreement with reported literature data [41–44]. Specifically, our results align closely with literature values for PAM2-I, PAM3-I, and PAM4-I determined spectrophotometrically at 25 °C and ionic strength of 0.15 mol kg^{-1} (7.92, 9.27, and 8.60, respectively) [41] as well as potentiometrically across different conditions: at 25 °C and I = 0.1 mol dm^{-3} (7.82, 9.10, and 8.23) [42]; at 25 °C and unspecified ionic strength (8.0, 9.2, and 8.6) [43]; and at 20 °C and unspecified ionic strength (8.00, 9.22, and 8.57) [44], respectively. This high degree of concordance confirms both the reliability of the applied methodology and the consistency of the acid–base behavior of *N*-methylpyridinium aldoximes across different experimental conditions. Furthermore, the

identical pK_a values obtained for PAM4-Cl and PAM4-I demonstrate that the counterion has no measurable effect on the acidity of the *para*-substituted aldoxime [25].

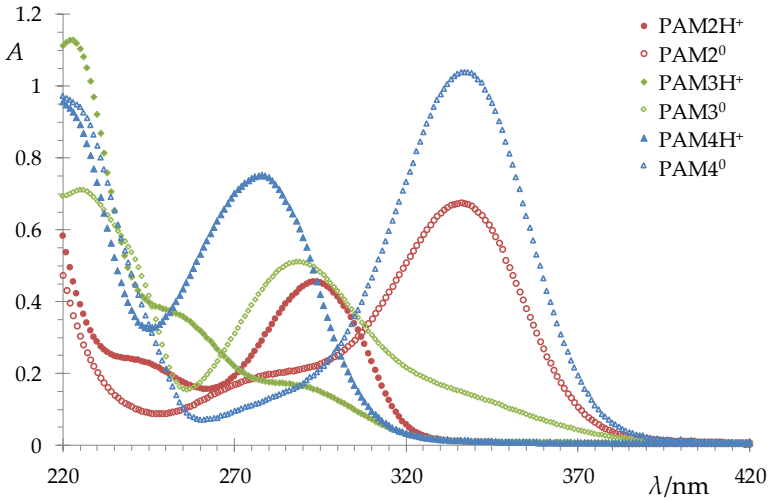

Figure 2. UV–Vis spectra of *N*-methylpyridinium aldoxime ionic forms ($c = 4 \times 10^{-5}$ mol dm^{-3}) at 25.0 °C and ionic strength $I = 0.10$ mol dm^{-3} ($PAMH^+$ at pH = 5.0; PAM^0 at pH = 11.3).

The established acidity order (*ortho* > *para* > *meta*) highlights the significance of charge delocalization and resonance stabilization in both the protonated ($PAMH^+$) and deprotonated, zwitterionic (PAM^0) forms of *N*-methylpyridinium aldoxime isomers. Notably, in the absence of resonance stabilization effects, the expected acidity trend would be *ortho* > *meta* > *para*, governed solely by the inductive electron-withdrawing effect of the positively charged pyridinium nitrogen atom [42,45].

The X-ray diffraction and spectroscopic data of PAM halides indicate a similar quinoid-like electron density distribution in the $PAM2H^+$ and $PAM4H^+$, which is distinctly different from that observed in $PAM3H^+$. The subtle structural differences are reflected in characteristic bond-length alternation patterns. Specifically, $PAM2H^+$ exhibits a "short–long–short–long" sequence along the C6–C5–C4–C3–C2 fragment (d(C6–C5) = 1.357(1) Å, d(C5–C4) = 1.377(1) Å, d(C4–C3) = 1.365(1) Å and d(C3–C2) = 1.386(1) Å) [38], indicative of π-electron localization. A comparable "short–long–long–short" pattern is observed for $PAM4H^+$ along the C5–C6–C2–C3–C4 fragment (d(C5–C6) = 1.377(2) Å, d(C6–C2) = 1.399(1) Å, d(C2–C3) = 1.401(1) Å and d(C3–C4) = 1.376(2) Å) [25]. In contrast, the nearly uniform bond lengths observed for the C4–C5–C6–C2–C3 fragment of $PAM3H^+$ (d(C4–C5) = 1.370(4) Å, d(C5–C6) = 1.372(4) Å, d(C6–C2) = 1.381(3) Å and d(C2–C3) = 1.378(3) Å, Table S2) are consistent with the pronounced π-electron delocalization within the pyridinium ring. Analysis of bond lengths in the oxime group provides additional insight. Compared with $PAM3H^+$, both $PAM2H^+$ (d(C1–N1) = 1.274(1) Å and d(N1–O1) = 1.372(1) Å) [38] and $PAM4H^+$ (d(C1–N1) = 1.280(1) Å and d(N1–O1) = 1.382(1) Å) [25] exhibit longer C1–N1 bonds accompanied by shorter N1–O1 bonds, consistent with the enhanced single-bond character of the C=N bond and a partial double-bond character of the N–O bond. Furthermore, in $PAM3H^+$, the C1–N1 and N1–O1 bond lengths (d(C1–N1) = 1.259(3) Å and d(N1–O1) = 1.386(3) Å) indicate a higher degree of double-bond character of the oximic carbon–nitrogen bond and a reduced π-contribution to the nitrogen–oxygen bond. For $PAM2H^+$ and $PAM4H^+$, π-electron localization within the pyridinium ring is accompanied by a C2=C1–N1=O1$^+$H electron distribution within the oxime group, whereas in $PAM3H^+$, delocalization within the pyridinium ring coincides with a C2–C1=N1–O1H arrangement in the aldoxime fragment (Figure 3).

https://doi.org/10.3390/ijms27042015

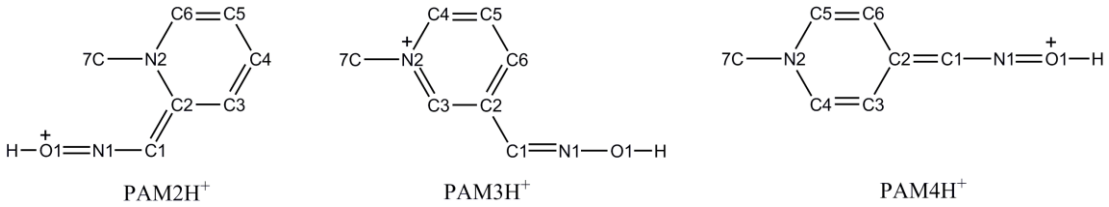

Figure 3. Presumed electron distribution patterns within the protonated form of *N*-methylpyridinium aldoxime isomers. Carbon-bound hydrogen atoms are omitted for clarity.

The described electronic distributions—namely, R=C(H)–N=O⁺H in the *ortho*- and *para*-isomers and R⁺–C(H)=N–OH in the *meta*-isomer—together with the observed acidity trend across the PAMH⁺ series, are further corroborated by ^{1}H NMR and IR spectroscopy (Section 3.3). The hydroxyl proton chemical shifts follow the order δ(PAM2H⁺) = 13.33 ppm > δ(PAM4H⁺) = 12.73 ppm > δ(PAM3H⁺) = 12.22 ppm. The pronounced downfield shift observed for PAM2H⁺ reflects stronger deshielding of the oximic hydroxyl proton, indicating the greater contribution of the R=C(H)–N=O⁺H resonance structure compared with PAM4H⁺ and PAM3H⁺. Furthermore, in PAM2-Cl, the R=C(H)–N=O⁺H electronic distribution leads to lower C=N and higher N–O stretching frequencies [46], as was confirmed by IR spectroscopy.

The established acidity order is also consistent with the resonance effects proposed for the zwitterions. In the *ortho*- (PAM2^0) and *para*- (PAM4^0) isomer, the quinoid resonance structure, which exhibits no charge separation, is expected to have a considerable contribution to the resonance hybrid (Figure S5). Thus, within PAM2^0 and PAM4^0, the oximic C=N bond is expected to exhibit increased single-bond character accompanied by partial double-bond character of the N–O bond, which agrees with an electronic distribution that corresponds to the R=CH–N=O motif. In contrast, for the *meta*-isomer, only charge-separated resonance structures are possible, resulting in reduced stabilization of the zwitterionic form (Figure S5). This is supported by the calculated bond lengths in the PAM zwitterions (Table S5; see ESI).

The close correspondence between the bond-length patterns obtained from X-ray diffraction and those calculated by DFT (in an implicit solvent model; Section 2.3) demonstrates that the observed structural features are primarily dictated by intrinsic electronic effects rather than by crystal-packing forces. This confirms that the quinoid-like character of the *ortho*- and *para*-isomers is a fundamental property of their π-electron systems.

Finally, the difference in the electronic structure of the examined *N*-methylpyridinium aldoxime isomers is evident from their UV–Vis spectral features. The close similarity between the UV–Vis spectra of the *ortho*- and *para*-isomers, contrasted with the distinctly different spectrum of the *meta*-isomer (Figure 2), provides further evidence for analogous electron density distributions in PAM2 and PAM4, and a fundamentally different electronic structure in PAM3. Collectively, these results demonstrate that resonance effects play a decisive role in governing the acidity, electronic structure, and spectroscopic properties of *N*-methylpyridinium aldoximes. To support these experimental findings, a comparative DFT study was performed, providing in-depth insight into distinct electronic effects involved (Section 2.3).

2.2. Pentacyano(N-methylpyridinium aldoxime)ferrate(II) Complexes

2.2.1. UV–Vis Spectroscopy

The UV–Vis spectra of the in situ-produced pentacyano(PAM)ferrate(II) complexes were recorded in buffered aqueous solutions over the pH range 5–11.5 when the equilibrium was reached. In all cases, the spectra are dominated by a moderately intense absorption band in the visible region, which shows only a weak dependence on pH. This band

is assigned to a metal-to-ligand charge-transfer (MLCT) transition of $d_{\pi}(Fe^{II}) \rightarrow p_{\pi^*}(PAM)$ character. For complexes containing the protonated ligand forms, the MLCT band maxima are observed at 523 nm for $PAM2H^+$, 467 nm for $PAM3H^+$, and 558 nm for $PAM4H^+$ (Figure 4). Notably, the energy of this transition remains largely invariant upon changes in pH, indicating that deprotonation of the oxime group does not significantly perturb the electronic coupling between the metal center and the ligand π-system. Nevertheless, subtle but systematic shifts can be discerned: increasing pH induces a small red shift for the PAM2 (~20 nm) and PAM4 (~10 nm) complexes, whereas a minor blue shift (~5 nm) is observed for the PAM3 complex (Figure S6). These trends further reflect differences in the electronic structure of the ligands and are fully consistent with the aforementioned similar electron density distributions for the *ortho*- and *para*- isomers, in contrast to the *meta*-isomer. Accordingly, the MLCT band positions of the pentacyano(PAM2)ferrate(II) and pentacyano(PAM4)ferrate(II) complexes are more closely related to each other than to the pentacyano(PAM3)ferrate(II) analogue, supporting the conclusions drawn from the UV–Vis, NMR, and crystallographic analyses of the free ligands.

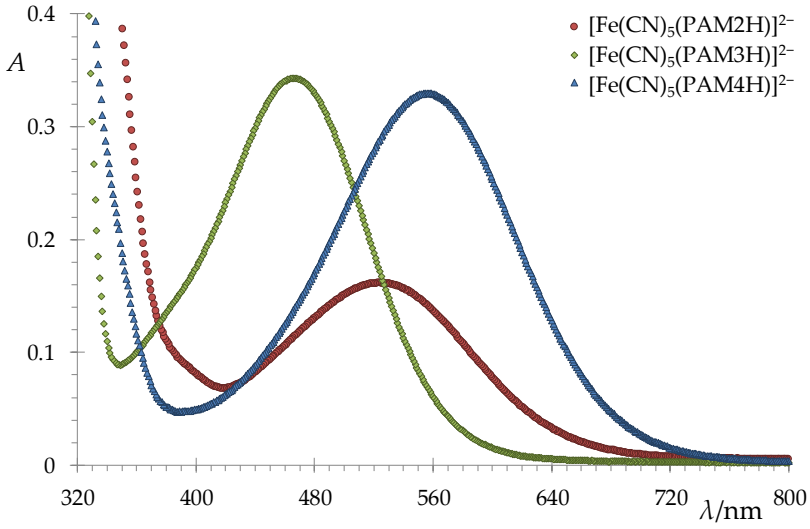

Figure 4. The UV–Vis spectra of pentacyano(*N*-methylpyridinium aldoxime)ferrate(II) complexes at 25.0 °C, ionic strength I = 0.10 mol dm^{-3}, and pH = 6.06. $c_0([Fe(CN)_5(H_2O)]^{3-})$ = 2 × 10^{-4} mol dm^{-3}, $c_0(PAMH^+)$ = 2 × 10^{-3} mol dm^{-3}, c_0(L-ascorbic acid) = 4 × 10^{-4} mol dm^{-3}.

2.2.2. Kinetic Studies

The formation of the pentacyano(*N*-methylpyridinium aldoxime)ferrate(II) complexes from aquapentacyanoferrate(II) can be represented by

$$[Fe(CN)_5(H_2O)]^{3-}(aq) + PAMH_n^{n+}(aq) \xrightarrow{k_f} [Fe(CN)_5(PAMH_n)]^{(3-n)-}(aq) + H_2O(l)$$

where n equals 1 for the protonated ($PAMH^+$) or 0 for the deprotonated (PAM^0) ligand. The influence of the *N*-methylpyridinium aldoxime isomerism on the reactivity towards $[Fe(CN)_5(H_2O)]^{3-}$ is clearly evident from the experimentally determined formation rate constants (Table 1). The observed decrease in k_f values for $[Fe(CN)_5(PAMH)]^{2-}$ complexes in the order *meta* > *para* > *ortho* can be rationalized primarily in terms of increasing steric hindrance at the coordination site. This interpretation is further supported by the degree of nonplanarity of the protonated ligands. Computational data show that $PAM2H^+$ exhibits the largest deviation from planarity, with a C(pyridinium)–C(oxime) torsion angle of approximately 25°, whereas $PAM3H^+$ and $PAM4H^+$ remain close to planar. The increased torsion in $PAM2H^+$ reduces the steric accessibility of the oxime nitrogen atom and hinders its approach to the metal center, resulting in a substantially lower formation rate constant.

A direct correlation between the formation rate constants and the torsion angles of the protonated ligands is summarized in Table S6. In addition, the k_f values reported herein are considerably lower than those reported for other pentacyano(ligand)ferrates(II) with monocationic ligands [34,47]. The unexpectedly small contribution of the positive charge in the case of *N*-methylpyridinium aldoximes can be attributed to charge delocalization within the ligand framework and to the spatial separation between the quaternary pyridinium nitrogen atom and the coordinating oxime group. Additionally, their relatively low reactivity may also be associated with the *E*-configuration of the ligand functional group, which can impose a sterically unfavorable orientation for coordination, as previously suggested for certain pyridinecarbonyloximes [48].

Semi-quantitative monitoring of the complex formation reactions over the pH range 5–11.5 indicated a pH dependence of the formation rates. Under alkaline conditions, the time required to reach equilibrium was noticeably longer. Presumably, the ionization of the ligands reduces their electrostatic attraction toward the negatively charged pentacyanoferrate(II) moiety, thereby decreasing the rate of complex formation.

Table 1. Formation and dissociation kinetic parameters, and formation equilibrium constants of pentacyano(*N*-methylpyridinium aldoxime)ferrate(II) complexes.

$[Fe(CN)_5(PAM2H_n)]^{(3-n)-}$		**$[Fe(CN)_5(PAM3H_n)]^{(3-n)-}$**		**$[Fe(CN)_5(PAM4H_n)]^{(3-n)-}$**	
Formation rate constant					
(ϑ = (24.7 ± 0.2) °C; pH = 5.98 ± 0.02; I = 0.10 mol dm^{-3})					
λ_{MLCT} (nm)	k_f (dm^3 mol^{-1} s^{-1})	λ_{MLCT} (nm)	k_f (dm^3 mol^{-1} s^{-1})	λ_{MLCT} (nm)	k_f (dm^3 mol^{-1} s^{-1})
523	4.15 ± 0.04	467	48.84 ± 1.21	558	26.72 ± 0.37
Dissociation rate parameters					
(ϑ = (24.8 ± 0.2) °C; I = 0.10 mol dm^{-3})					
$k_{d1} \times 10^3$ (s^{-1})	$k_{d2} \times 10^3$ (s^{-1})	$k_{d1} \times 10^3$ (s^{-1})	$k_{d2} \times 10^3$ (s^{-1})	$k_{d1} \times 10^3$ (s^{-1})	$k_{d2} \times 10^3$ (s^{-1})
17.9	7.9	27.8	18.2	16.9	4.6
pK_a(coord. PAM2H$^+$)		pK_a(coord. PAM3H$^+$)		pK_a(coord. PAM4H$^+$)	
9.58		10.47		9.39	
Activation parameters of dissociation					
(pH = 6.05 ± 0.01; I = 0.10 mol dm^{-3})					
$\Delta H^‡$ (kJ mol^{-1})	$\Delta S^‡$ (J K^{-1} mol^{-1})	$\Delta H^‡$ (kJ mol^{-1})	$\Delta S^‡$ (J K^{-1} mol^{-1})	$\Delta H^‡$ (kJ mol^{-1})	$\Delta S^‡$ (J K^{-1} mol^{-1})
107.1 ± 3.1	79.1 ± 7.5	94.5 ± 2.3	40.8 ± 6.7	105.3 ± 5.0	73.9 ± 16.0
Equilibrium constant					
(ϑ = (24.8 ± 0.1) °C; pH = 6.01 ± 0.03; I = 0.10 mol dm^{-3})					
log (K/dm^3 mol^{-1})		log (K/dm^3 mol^{-1})		log (K/dm^3 mol^{-1})	
2.38 ± 0.02		3.24 ± 0.02		3.21 ± 0.02	

The dissociation of pentacyano(PAM)ferrate(II) complexes was investigated in the presence of DMSO, employed as a scavenger ligand that forms a stable and substitution-inert complex with $[Fe(CN)_5]^{3-}$ [49]. The dissociation kinetics were found to be pH-dependent due to the ligand ionization (Table S7 and Figure S7). The overall process can be represented by the following reaction scheme.

$$[Fe(CN)_5(PAMH)]^{2-} \overset{K_{a\ coord.}}{\rightleftarrows} [Fe(CN)_5(PAM)]^{3-} + H^+$$

$$[Fe(CN)_5(PAMH)]^{2-} + DMSO \overset{k_{d1}}{\longrightarrow} [Fe(CN)_5(DMSO)]^{3-} + PAMH^+$$

$$[Fe(CN)_5(PAM)]^{3-} + DMSO \overset{k_{d2}}{\longrightarrow} [Fe(CN)_5(DMSO)]^{3-} + PAM^0$$

https://doi.org/10.3390/ijms27042015

Although the dissociation rate constants are of comparable magnitude for all complexes (Table S7), several conclusions can nevertheless be drawn. At all investigated pH values, the complex with the coordinated *meta*-isomer is the most labile, whereas the complexes with *ortho*- and *para*-isomer exhibit nearly identical labilities. The activation parameters determined for the dissociation of $[Fe(CN)_5(PAMH)]^{2-}$ complexes (Table 1; data in Table S8) fall within the range typical for pentacyano(ligand)ferrates(II) and are fully consistent with the limiting dissociative (D) mechanism [34,47], as inferred from the activation parameters and in agreement with the established behavior of pentacyanoferrate(II) complexes. Analysis of the k_d values indicates that the σ-donor character of the investigated *N*-methylpyridinium aldoximes outweighs their π-acceptor ability. However, among these, both *ortho*- and *para*-isomer exhibit comparable and stronger π-acceptor properties than the *meta*-isomer. This is supported by the highest dissociation rate constant, the highest MLCT transition energy, and the lowest activation enthalpy for dissociation observed for the pentacyano(PAM3)ferrate(II) complex. In contrast, the close similarity of k_d, λ_{MLCT}, and $\Delta H^{\ddagger}$ values for the pentacyano(PAM2)ferrate(II) and pentacyano(PAM4)ferrate(II) complexes reflects an analogous π-acceptor strength of PAM2 and PAM4. Similar correlations between π-acceptor properties and kinetic and spectroscopic parameters have been reported for a variety of N-heterocyclic ligands [50–52].

The observed pH dependence of both spectral and kinetic parameters is consistent with the coordination of *N*-methylpyridinium aldoxime ligands to the pentacyanoferrate(II) via the oxime nitrogen atom. The absence of substantial changes in the MLCT band energy upon ligand deprotonation indicates that the coordination mode remains unchanged across the investigated pH range. Coordination through the oxygen atom would be expected to result in either the disappearance of the MLCT band or its pronounced shift with increasing pH. Moreover, N-coordination is further supported by the small differences between dissociation rate constants for complexes with protonated and deprotonated ligands, and between the ionization constants of free and coordinated ligands (Tables 1 and S4). In contrast, significantly larger differences between k_{d1} and k_{d2}, and a greater change in the oxime ionization constant, would be anticipated for O-coordinated aldoximes.

The stability constants of the $[Fe(CN)_5(PAMH)]^{2-}$ complexes were determined by calculating the ratio of the formation and dissociation rate constants at pH = 6.0 and are reported as log (K/dm^3 mol^{-1}) in Table 1. With values on the order of 10^2–10^3 dm^3 mol^{-1}, these complexes are less stable than most reported pentacyano(ligand)ferrate(II) complexes with N- and S-donor ligands, which typically reach magnitudes of 10^5–10^6 dm^3 mol^{-1} [34,47]. Moreover, their stability is comparable to that of several complexes containing amino acids [34,47]. Among the pentacyano(PAM)ferrates(II), the complex containing the *ortho*-isomer exhibits the lowest stability, which can be attributed to the steric destabilization arising from the vicinal arrangement of the methyl and oxime groups.

These findings collectively demonstrate how subtle variations in ligand structure and electronic properties govern both the kinetic and thermodynamic behavior of pentacyanoferrate(II) complexes with *N*-methylpyridinium aldoximes.

2.3. Computational Analysis

To rationalize and provide molecular-level insight into the experimentally observed trends in acid–base properties, spectral features, and complex stability of the investigated *N*-methylpyridinium aldoximes and their pentacyanoferrate(II) complexes, a comprehensive DFT study was performed. In particular, the calculations were used to elucidate charge redistribution effects, solvation contributions, and structural distortions upon coordination, which cannot be directly inferred from experimental data alone.

2.3.1. Geometry, Protonation State, and Acidity

All PAM ligands (PAM2, PAM3, and PAM4) were optimized in both their cationic ($PAMH^+$) and neutral (PAM^0) protonation states, as well as in their corresponding pentacyanoferrate(II) complexes. The optimized geometries reveal that all cationic ligands adopt predominantly planar conformations (Table S9), allowing efficient π-conjugation between the pyridinium ring and the oxime group. An exception is $PAM2H^+$, where steric interactions in the *ortho* position lead to a pronounced rotation of 25° around the central C(pyridinium)–C(oxime) bond. This structural distortion destabilizes the protonated $PAM2H^+$ form and is consistent with its experimentally and computationally determined higher acidity. Upon deprotonation, all ligands relax into more planar geometries, reflecting enhanced delocalization of the π-electron system. This pronounced rotation is consistent with the markedly reduced formation rate constant of the $PAM2H^+$ complex and supports a steric origin of the kinetic trend.

The computed pK_a values for $PAM2H^+$, $PAM3H^+$, and $PAM4H^+$ are 7.9, 10.2, and 9.1, which align well with the experimental 7.97, 9.42, and 8.56 (Tables S4 and S9), respectively. The calculated data reproduce both the magnitude and the experimentally observed acidity trend, $PAM2H^+ > PAM4H^+ > PAM3H^+$, confirming the reliability of the computational model and its consistency with the spectrophotometric data.

2.3.2. Charge Distribution and Coordination Ability

The described structural changes induced by deprotonation are accompanied by pronounced redistribution of electron density, which directly impacts coordination ability and complex stability (Table S9). Atomic charge distribution analysis provides important insight into the coordination behavior of PAM ligands. Based solely on atomic charges, the oxime oxygen appears substantially more nucleophilic than the corresponding nitrogen atom, carrying approximately four- to six-fold-higher negative charge. However, as Fe(II) is a borderline Lewis acid, it preferentially coordinates N-, P-, and S-donor atoms over O-donors, in agreement with the experimentally inferred coordination mode.

More revealing trends emerge upon analysis of charge redistribution following oxime –OH deprotonation. Although the negative charge on the oxygen atom increases as expected, it accounts for only about 10–20% of the newly generated charge, indicating extensive delocalization. Consequently, 80–90% of the excess charge is redistributed over other parts of the molecule via resonance. Importantly, this charge is not transferred to the coordinating oxime nitrogen atom; instead, this atom becomes even less electron-rich upon deprotonation. Specifically, the charge on the coordinating nitrogen in $PAM2H^+$, $PAM3H^+$, and $PAM4H^+$ changes from −0.10, −0.14, and −0.11 to −0.06, −0.13, and −0.08, respectively. A significant fraction of the negative charge (around 15–18%) is localized on the oxime carbon atom.

Charge transfer into the pyridinium ring is limited, amounting to approximately 12% in PAM3 and up to 20% in PAM2. Accordingly, the charge on the pyridinium nitrogen changes by only around 4% in $PAM2H^+$ and $PAM4H^+$, while remaining essentially unchanged in $PAM3H^+$, which is consistent with the absence of resonance interaction in the *meta*-substituted isomer. Overall, most of the newly generated negative charge remains within the oxime fragment, but not on the nitrogen atom that ultimately coordinates to the Fe(II) center in the pentacyano(PAM)ferrate(II) complexes. Consequently, despite the formally increased nucleophilicity of the deprotonated ligand, its actual σ-donor ability towards Fe(II) is reduced. This counterintuitive effect provides an explanation for the theoretically observed decrease in complex stability at higher pH values, where deprotonated PAM^0 forms dominate. In addition, solvation calculations indicate significantly stronger stabilization of the isolated neutral (zwitterionic) ligands in aqueous solution. This enhanced solvation, combined with the reduced donor strength of the coordinating N-atom,

is fully consistent with the observed lower stability of complexes involving neutral ligands.

This analysis reveals that the counterintuitive decrease in complex stability at higher pH values is not a simple consequence of reduced electrostatic attraction, but originates from delocalization of the negative charge away from the coordinating nitrogen atom and from enhanced solvation of the zwitterionic ligands, effects that cannot be deduced from experimental observables alone.

2.3.3. Electronic Structure and UV–Vis Properties

Time-dependent DFT (TD-DFT) calculations were used to simulate the electronic absorption spectra of the free PAM ligands (Table 2). The calculated spectra show excellent agreement with the experimentally recorded UV–Vis spectra discussed in Section 2.1.2, in terms of both band positions and relative intensities, thus validating the applied computational methodology.

Table 2. Computed UV–Vis spectra of different protonation forms of investigated ligands using the TD-DFT approach and the (SMD)/CAM-B3LYP/6–311++G(d,p) model in water. Experimental λ_{max} values reported here are presented in square brackets and are given for comparison.

Computed UV–Vis Spectra	Ligand	λ_{max}	Oscillator Strength	Hole Orbital	Particle Orbital
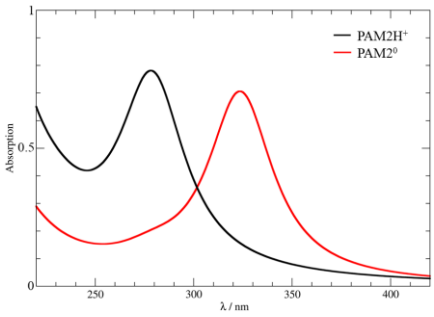	PAM2H$^+$	278 nm [293 nm]	f = 0.6888	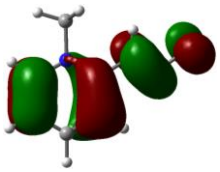 HOMO	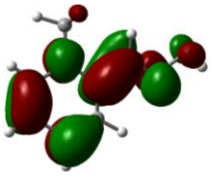 LUMO
	PAM2^0	324 nm [335 nm]	f = 0.6765	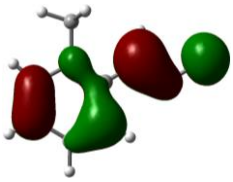 HOMO	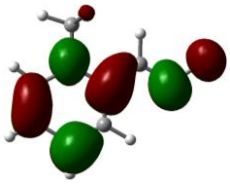 LUMO
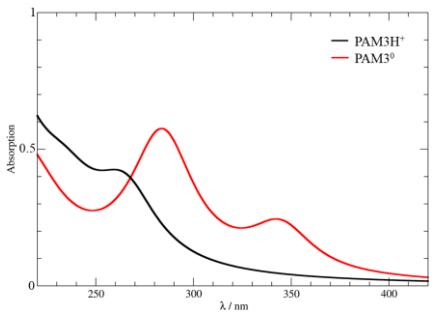	PAM3H$^+$	259 nm [256 nm]	f = 0.2715	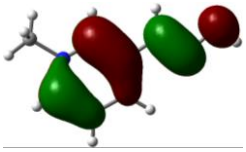 HOMO	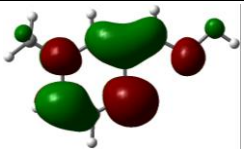 LUMO
	PAM3^0	284 nm [288 nm]	f = 0.4962	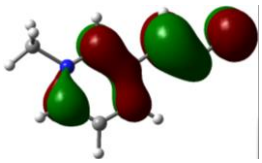 HOMO	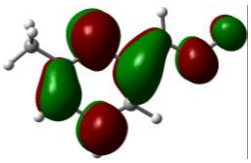 LUMO+1
		342 nm [340 nm]	f = 0.1866	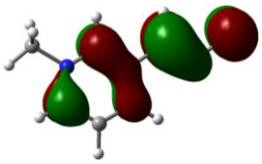 HOMO	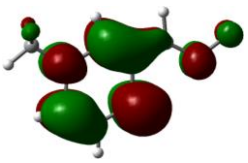 LUMO

https://doi.org/10.3390/ijms27042015

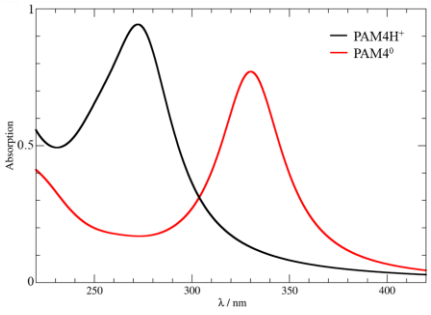

$PAM4H^+$	274 nm [279 nm]	$f = 0.7703$	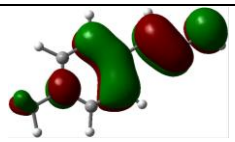 HOMO	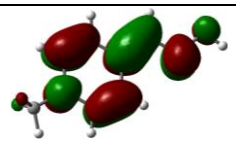 LUMO
$PAM4^0$	330 nm [337 nm]	$f = 0.7454$	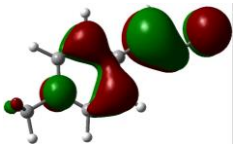 HOMO	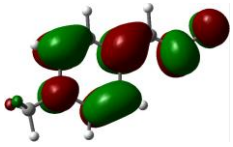 LUMO

For PAM2 and PAM4, in both of their protonation forms, the dominant absorption band arises from a single π–π* transition of predominantly HOMO→LUMO character. In contrast, $PAM3^0$ exhibits two distinct absorption bands that arise from HOMO→LUMO transition at 342 nm and HOMO→LUMO+1 transition at 284 nm. Both transitions are of π–π* character, reflecting the unique electronic structure of the *meta*-isomer, which is also reflected in the MLCT band positions of the corresponding pentacyano(PAM)ferrate(II) complexes (Section 2.2.1).

We note that we did not attempt to model the UV–Vis spectra of the pentacyano(PAM)ferrate(II) complexes in the region above 450 nm, despite employing the range-separated CAM-B3LYP functional with the large 6-311++G(d,p) basis set, because this approach was unable to reproduce the experimentally observed low-energy transitions. Although CAM-B3LYP generally improves the description of long-range charge-transfer excitations compared to conventional hybrid functionals, it remains limited for transitions with pronounced metal-centered (MC) character or mixed MLCT/MC nature, and for spin-forbidden or weakly allowed excitations typical of low-spin d^6 Fe(II) cyanide complexes. Such deficiencies of TD-DFT have been clearly demonstrated by Schmidt and coworkers [30], who showed that even advanced functionals fail to accurately describe longer-wavelength excitations in related Fe(II) systems due to the multiconfigurational nature of the excited states and insufficient treatment of electronic correlation. Consequently, the experimentally observed features above 450 nm remain outside the reliable predictive scope of the applied computational model.

2.3.4. Stability of Pentacyano(PAM)ferrate(II) Complexes

The stability of all examined complexes between the pentacyanoferrate(II) anion and PAM ligands was computed as the reaction Gibbs free energy (ΔG_R) for the ligand-exchange process according to the following chemical equation:

$$[Fe(CN)_5(H_2O)]^{3-} + PAMH_n^{n+} \rightleftarrows [Fe(CN)_5(PAMH_n)]^{(3-n)-} + H_2O + \Delta G_R$$

The obtained results (Table 3) reveal a clear stability trend among the protonated ligands—$PAM3H^+ \approx PAM4H^+ > PAM2H^+$—with $PAM2H^+$ forming the least stable complex. This ordering mirrors the stability deduced from the experimentally observed trends in formation and dissociation kinetics. In the case of $PAM2H^+$, the close proximity of the *N*-methyl group and the oxime moiety leads to pronounced ligand distortion upon coordination, manifested as a rotation of 72° around the central C(pyridinium)–C(oxime) bond, representing a 47° increase relative to the isolated ligand. This geometric penalty is the crucial reason for the markedly lower stability of the $PAM2H^+$ complex (ΔG_R = −2.8 kcal mol^{-1}). In $PAM3H^+$, the spatial separation of these groups significantly reduces this effect, resulting in a smaller rotation angle of 47° and a substantially more stable complex (ΔG_R = −4.8 kcal mol^{-1}). $PAM4H^+$ forms a complex with an essentially extended geometry; however, enhanced resonance interaction with the *para*-*N*-methyl group and reduced

nucleophilicity of the coordinating nitrogen limit the stability gain, yielding only a marginally more stable complex than PAM3H$^+$ (ΔG_R = −5.0 kcal mol^{-1}). Additionally, the enhanced stability of the PAM3H$^+$ and PAM4H$^+$ complexes is further supported by the formation of intramolecular hydrogen bonds between the oxime –OH group and one of the cyanide ligands of the pentacyanoferrate(II) moiety (Table 3).

All neutral ligands form significantly less stable complexes, a counterintuitive result that is fully consistent with the previously discussed charge-distribution analysis and reduced coordination ability of the deprotonated forms. As mentioned, this does not occur due to unfavorable metal–ligand bonding or geometric mismatch, but primarily as a consequence of stronger solvation of the free ligands in their zwitterionic form.

All of these observations are consistent with the charge distribution following the ligand complexation (Table 3). In the reference complex $[Fe(CN)_5(H_2O)]^{3-}$, the calculated charge on the Fe(II) center is −0.72, while the combined charge of Fe(II) and the five cyanide ligands amounts to −3.20. Given the total charge of −3.00, this indicates a transfer of approximately 20% of one electronic charge from the coordinated water molecule to the pentacyanoferrate(II) fragment, providing a useful baseline for comparison.

Table 3. Optimized geometries of investigated pentacyano(PAM)ferrate(II) complexes with the (SMD)/M06-2X/6–311++G(d,p) model in water, together with relevant atomic charges (NBO analysis, in |e|), stability Gibbs free energies (ΔG_R, in kcal mol^{-1}), and pK_a values. Experimental values reported here are presented in square brackets and are given for comparison.

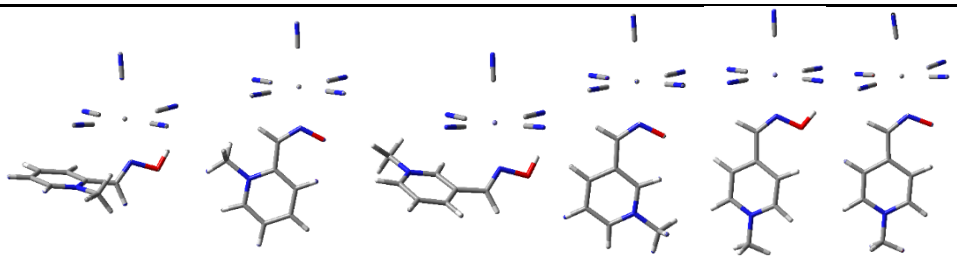

Fragment	$[Fe(CN)_5(H_2O)]^{3-}$	PAM2H$^+$	PAM2^0	PAM3H$^+$	PAM3^0	PAM4H$^+$	PAM4^0
Fe(II) ion	−0.72	−0.87	−0.87	−0.86	−0.87	−0.89	−0.87
$[Fe(CN)_5]^{3-}$ part	−3.20	−3.24	−3.31	−3.23	−3.32	−3.26	−3.32
N(aldoxime)	–	0.00	0.09	−0.02	0.05	0.02	0.08
O(aldoxime)	–	−0.54	−0.64	−0.58	−0.72	−0.56	−0.66
C(aldoxime)	–	0.08	−0.13	0.12	−0.06	0.09	−0.09
N(pyridine)	–	−0.31	−0.33	−0.32	−0.31	−0.31	−0.34
entire ligand	0.20	1.24	0.31	1.23	0.32	1.26	0.32
Stability (ΔG_R, kcal mol^{-1})	–	−2.8 [−3.2]	−2.6	−4.8 [−4.4]	−4.5	−5.0 [−4.4]	−4.6
pK_a	–	9.3 [9.58]		10.0 [10.47]		8.8 [9.39]	

In the corresponding complexes with PAM2H$^+$, PAM3H$^+$, and PAM4H$^+$, the Fe(II) charges increase to −0.87, −0.86, and −0.89, respectively, and the charge on the pentacyanoferrate(II) fragment increases to −3.24, −3.23, and −3.26. These results demonstrate that the PAM ligands are stronger electron donors than water, consistent with the feasibility of ligand substitution and the exergonic reaction Gibbs energies discussed above. While the overall increase in charge on the pentacyanoferrate(II) fragment is modest (3–6% of elementary charge), the charge localized on Fe(II) increases more substantially (14–17%). This discrepancy can be rationalized by the formation of hydrogen bonds between the nonionized oxime –OH group and a cyanide ligand, which reduces the ability of the cyanide group to withdraw electron density from the coordinated Fe(II) center.

https://doi.org/10.3390/ijms27042015

For the neutral (zwitterionic) PAM2, PAM3, and PAM4 ligands, similar but distinct trends are observed. In all three complexes, the charge on Fe(II) remains constant at −0.87, and the total charge of the pentacyanoferrate(II) fragment is −3.32. In contrast to the cationic systems, no intramolecular hydrogen bonding is formed between the deprotonated oxime group and cyanide ligands, resulting in comparable electron-withdrawing ability of the cyanide groups across all three complexes. Interestingly, despite their lower thermodynamic stability, the neutral ligands transfer more charge to the pentacyanoferrate(II) fragment, as reflected by a 6–9% higher negative charge relative to the $[Fe(CN)_5(PAMH)]^{2-}$ complexes. This apparent contradiction highlights that charge transfer alone does not determine complex stability; instead, the reduced stability of the $[Fe(CN)_5(PAM)]^{3-}$ complexes is attributed primarily to stronger solvation of the free ligands in their zwitterionic form, which disfavors the formation of more stable complexes during ligand substitution.

Finally, coordination significantly decreases the acidity of $PAM2H^+$ by 1.4 pK_a units relative to the free ligand, while slightly increasing the acidity of $PAM3H^+$ and $PAM4H^+$ by 0.2 and 0.3 pK_a units, respectively, again showing very good agreement with experimental pK_a values.

2.3.5. Correlation with Kinetic Observations

Electron density analyses of the optimized complexes confirm that the PAM ligands act as stronger electron donors than water molecules, supporting the experimentally observed feasibility of ligand substitution under pseudo-first-order conditions. While no explicit transition states were modeled, the computed donor strengths, solvation energies, and structural distortions provide a consistent explanation for the experimentally observed formation and dissociation rates.

Overall, the computational results provide a coherent molecular-level interpretation of the experimental findings presented in Sections 2.1 and 2.2. They demonstrate that the spectral properties, acid–base behavior, and kinetic stability of pentacyano(PAM)ferrate(II) complexes are governed by a subtle interplay of electronic structure, protonation state, intramolecular hydrogen bonding, and solvation effects, rather than by simple considerations of ligand nucleophilicity alone.

2.4. Implications for Oxime Antidote Design

Our results demonstrate that the physicochemical properties of *N*-methylpyridinium aldoximes—including an essential therapeutic agent—and their corresponding pentacyanoferrate(II) complexes, which serve as robust biomimetic models for iron-containing proteins, are highly dependent on their positional isomerism. Significant pK_a shifts and isomer-specific charge-transfer variations can be directly correlated with the orientation and nucleophilic strength of the oxime group within the AChE active site, as modeled by the PDB (Protein Data Bank) 2GYU structure [53]. The lower pK_a of $PAM2H^+$ ensures a higher concentration of the nucleophilic oximate form at the physiological pH of 7.4, which is a prerequisite for the reactivation of OP-inhibited AChE. The pronounced localization (quinoid character) observed for PAM2 and PAM4 might influence the nucleophilic "hardness" of the oxygen atom, a factor that could be tuned in the design of future antidotes. The use of the $[Fe(CN)_5]^{3-/2-}$ moiety as a probe for biological macromolecules is well-established, particularly in studying electron-transfer pathways in cytochrome *c* and other heme-containing proteins [47]. The novel findings regarding the substitution kinetics and electronic transitions observed in $[Fe(CN)_5(PAMH_n)]^{(3-n)-}$ systems offer not only a model for how pyridinium-based antidotes might interact with transition metal centers, but also reveal how the coordination environment modulates the pK_a and nucleophilicity of the oxime group. This provides a chemical rationale for how metal-binding could modulate the clinical efficacy of AChE reactivators.

https://doi.org/10.3390/ijms27042015

3. Materials and Methods

3.1. Materials

PAM2-Cl was obtained from Sigma-Aldrich and employed as received. The starting chemicals for the synthesis of PAM3-I, PAM4-I, and sodium amminepentacyanoferrate(II) trihydrate were reagent-grade Acros Organics (Geel, Belgium) or Sigma-Aldrich (Darmstadt, Germany) products and were used as purchased.

The solutions of aquapentacyanoferrate(II), $[Fe(CN)_5(H_2O)]^{3-}$, were freshly prepared by dissolving $Na_3[Fe(CN)_5(NH_3)]\cdot 3H_2O$ in water at room temperature and stored in the dark to minimize the thermal and photolytic decomposition. To all reaction mixtures used for kinetic experiments, L-ascorbic acid (Sigma-Aldrich) was added to prevent metal center oxidation [54–56]. Dimethyl sulfoxide (DMSO, Sigma-Aldrich) was used as purchased in kinetic experiments.

Constant pH of the aqueous solutions was maintained with Britton–Robinson buffers, prepared by mixing 25 cm^3 of phosphoric, boric, and acetic acid solution (c = 0.0400 mol dm^{-3} for each acid) with different volumes of 0.2000 mol dm^{-3} sodium hydroxide solution [57]. A constant ionic strength was adjusted with 0.50 mol dm^{-3} sodium chloride solution. Deionized water was used throughout. For experiments involving Fe(II), water, buffers and stock solutions were previously purged with nitrogen.

3.2. Instruments

The UV–Vis measurements were performed on a Varian Cary Bio 100 spectrophotometer (Varian, Palo Alto, CA, USA) with thermostated cell holders (Dual Cell Peltier Accessory thermostat) in 1-cm quartz cuvettes. IR spectra (KBr pellets) were recorded on a Perkin Elmer Spectrum GX Series S spectrometer (PerkinElmer, Waltham, MA, USA) in the 4000–400 cm^{-1} range.

The ^1H and ^{13}C NMR data were collected at room temperature on a Bruker Avance 600 spectrometer (Bruker, Billerica, MA, USA) operating at 300.133 MHz for the ^1H nucleus and 75.447 MHz for the ^{13}C nucleus. Spectra were recorded in DMSO-d_6, and tetramethylsilane was used as the internal standard. ^1H and ^{13}C chemical shifts are assigned according to the atom numbering presented in Figure 5.

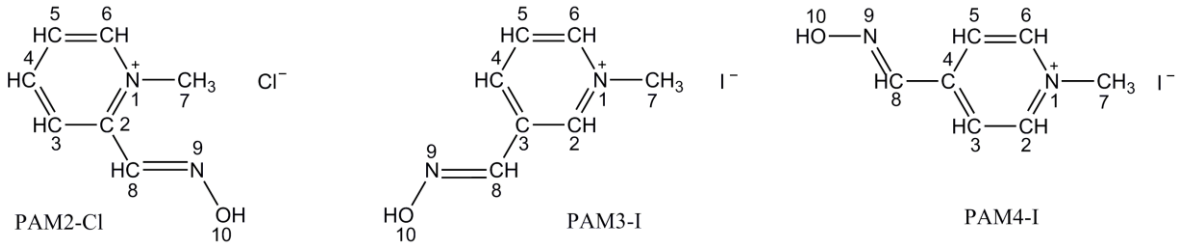

Figure 5. Labelling scheme for PAM2-Cl, PAM3-I, and PAM4-I used for NMR assignments.

Elemental analysis was conducted on a LECO elemental analyzer (LECO Corporation, St. Joseph, MI, USA) using the standardized ASTM D5291 method.

Purity analysis was performed using a coupled ultra-high-performance liquid chromatography–mass spectrometry–UV system (UHPLC–MS–UV) on a Waters Acquity UHPLC SQD-MS system (Agilent Technologies, Santa Clara, CA, USA) equipped with a UV detector set at 254 nm. Mass spectra were recorded in the range m/z 100–1000 using electrospray ionization (ESI) and a single-quadrupole detector.

Deionized water was prepared from distilled water using a MILLIPORE Simplicity™ Water Purification System (Merck, Darmstadt, Germany). The conductivity of the deionized water was 0.054 μS cm^{-1}.

The pH measurements were performed with a Mettler Toledo MA235 pH/Ion Analyzer pH meter (Mettler Toledo, Columbus, OH, USA) equipped with an InLab® Expert Pro pH electrode accurate to ±0.01 pH units.

3.3. Synthesis and Characterization of N-Methylpyridinium Aldoximes

The commercially available *N*-methylpyridinium-2-aldoxime chloride (PAM2-Cl) was characterized by IR and NMR spectroscopy, and its purity was confirmed by UHPLC–MS–UV. MS (*m*/*z*): calc. for $[C_7H_9N_2O]^+$ 137.07; found: 137.04. Selected IR data (cm^{-1}): ν(C=N)$_{oxime}$, 1628 (vs); ν(C–C, C–N)$_{pyridinium\ ring}$, 1595 (vs), 1581 (vs), 1504 (vs), 1440 (vs); ν(N–O)$_{oxime}$, 1011 (vs). ^{1}H NMR (DMSO-d_6, δ/ppm): 8.36 (d, J = 7.8 Hz, H-3), 8.54 (t, J = 7.9 Hz, H-4), 8.06 (t, J = 7.0 Hz, H-5), 9.12 (d, J = 6.1 Hz, H-6), 4.41 (s, 3 H, H-7), 8.68 (s, H-8), 13.33 (s, H-10). ^{13}C NMR (DMSO-d_6, δ/ppm): 147.5 (C-2), 124.7 (C-3), 141.4 (C-4), 127.0 (C-5), 146.5 (C-6), 46.0 (C-7), 144.8 (C-8).

N-methylpyridinium-3-aldoxime iodide (PAM3-I) was synthesized according to the following procedure. A solution of *E*-pyridine-3-aldoxime (5.70 mmol, Acros Organics) in 50 mL of acetone was prepared. Methyl iodide (1.42 cm^3, 22.8 mmol, Sigma-Aldrich) was added and the reaction mixture was stirred at room temperature for approximately 8 h and then left to stand overnight at 4 °C, affording pale yellow crystals of the *E*-isomer of *N*-methylpyridinium-3-aldoxime iodide. The product was collected by vacuum filtration, washed with cold acetone and dried under reduced pressure in a desiccator over phosphorus(V) oxide for approximately 8 h. Yield: 72%. *Anal*. Calc. for $C_7H_9N_2OI$: C, 31.84; H, 3.44; N, 10.61%. Found: C, 31.89; H, 3.42; N, 10.54%. MS (*m*/*z*): calc. for $[C_7H_9N_2O]^+$ 137.07; found: 137.08. Selected IR data (cm^{-1}): ν(C=N)$_{oxime}$, 1631 (m); ν(C–C, C–N)$_{pyridinium\ ring}$, 1584 (w), 1506 (vs), 1441 (s); ν(N–O)$_{oxime}$, 999 (vs). ^{1}H NMR (DMSO-d_6, δ/ppm): 9.20 (s, H-2), 8.69 (d, J = 8.2 Hz, H-4), 8.15 (dd, J_1 = 7.9 Hz, J_2 = 6.3 Hz, H-5), 8.96 (d, J = 6.1 Hz, H-6), 4.39 (s, 3 H, H-7), 8.36 (s, H-8), 12.22 (s, H-10). ^{13}C NMR (DMSO-d_6, δ/ppm): 143.3 (C-2), 133.2 (C-3), 128.0 (C-4), 141.4 (C-5), 143.1 (C-6), 48.5 (C-7), 145.4 (C-8).

N-methylpyridinium-4-aldoxime iodide (PAM4-I) was prepared according to a previously reported procedure [25]. A solution of *E*-pyridine-4-aldoxime (7.60 mmol, Sigma-Aldrich) in 15 mL of ethanol was prepared. Methyl iodide (1.89 mL, 30.40 mmol, Sigma-Aldrich) was added and the reaction mixture was stirred at room temperature for approximately 8 h and then left to stand overnight at 4 °C, affording yellow crystals of the *E*-isomer of *N*-methylpyridinium-4-aldoxime iodide. The product was collected by vacuum filtration, washed with cold ethanol and dried under reduced pressure in a desiccator over phosphorus(V) oxide for approximately 8 h. Yield: 45%. *Anal*. Calc. for $C_7H_9N_2OI$: C, 31.84; H, 3.44; N, 10.61%. Found: C, 31.84; H, 3.40; N, 10.65%. MS (*m*/*z*): calc. for $[C_7H_9N_2O]^+$ 137.07; found: 137.04. Selected IR data (cm^{-1}): ν(C=N)$_{oxime}$, 1643 (vs); ν(C–C, C–N)$_{pyridinium\ ring}$, 1611 (vs), 1572 (m), 1519 (vs); ν(N–O)$_{oxime}$, 996 (vs). ^{1}H NMR (DMSO-d_6, δ/ppm): 8.96 (d, J = 6.7 Hz, H-2, H-6), 8.21 (d, J = 6.8 Hz, H-3, H-5), 4.33 (s, 3 H, H-7), 8.43 (s, H-8), 12.73 (s, H-10). ^{13}C NMR (DMSO-d_6, δ/ppm): 145.0 (C-2, C-6), 123.6 (C-3, C-5), 147.8 (C-4), 47.6 (C-7), 145.7 (C-8).

The obtained ^{1}H and ^{13}C NMR chemical shifts for PAM2-Cl, PAM3-I, and PAM4-I were found to be in good agreement with those published [44,58,59]. Their purity, ranging from 96.0 to 99.9%, was confirmed by UHPLC–MS–UV analysis.

3.4. Synthesis of Sodium Amminepentacyanoferrate(II) Trihydrate

Sodium amminepentacyanoferrate(II) trihydrate, $Na_3[Fe(CN)_5(NH_3)]\cdot 3H_2O$, was synthesized from sodium nitroprusside dihydrate (Sigma-Aldrich) and recrystallized following the procedure reported in the literature [60]. Sodium acetate (0.040 mol) was dissolved in 40 cm^3 of aqueous ammonia ($w(NH_3) > 25\%$), and the solution was cooled in an ice bath. Finely ground $Na_2[Fe(CN)_5(NO)]\cdot 2H_2O$ (0.030 mol) was then added, and the mixture was

stirred for 90 min while maintained in the ice bath. The reaction mixture was kept at 4 °C for 5 h, after which the product was separated by filtration. The product was dissolved in 20 cm^3 of water, and filtered to remove insoluble impurities. Mixing the filtrate with 20 cm^3 of cold ethanol afforded a precipitate, which was collected by vacuum filtration, washed with cold ethanol, dried under reduced pressure in a desiccator over phosphorus(V) oxide and stored in a dark bottle under a nitrogen atmosphere in a desiccator. Yield: 55%. *Anal.* Calc. for $Na_3FeC_5N_6H_9O_3$: C, 18.42; H, 2.78; N, 25.78%. Found: C, 18.52; H, 2.64; N, 25.53%. IR (cm^{-1}): ν(N–H, O–H), ~3450 (vs, br), 3289 (vs); ν(C≡N), 2043 (vs), 2014 (vs); $\delta(NH_3)$, 1647 (vs), 1259 (vs), 671 (m); $\delta(H_2O)$, 1620 (vs); δ(Fe–C≡N), 574 (vs); ν(Fe–CN), 503 (m). The IR data are consistent with the reported values [61].

3.5. X-Ray Crystallography

The single crystal X-ray diffraction data of a suitable crystal of PAM3-I were collected on an Oxford Diffraction Xcalibur diffractometer (Oxford Diffraction Ltd., Abingdon, Oxfordshire, UK) with a Sapphire 3 CCD detector and Mo Kα radiation. The crystal was kept at 293(2) K during data collection. The CrysAlis Software system, Version 171.37.33 [62], was used for data collection and reduction. The multi-scan procedure was used for absorption effects. Using Olex2 [63], the structure was solved by direct methods with the SHELXS [64] program and refined with the SHELXL [65] refinement package using least-squares minimization. Anisotropic displacement parameters for all nonhydrogen atoms were included. The positions of hydrogen atoms belonging to the carbon atoms were geometrically optimized applying the riding model [Csp^2–H 0.93 Å, U_{iso}(H) = 1.2U_{eq}(C); Csp^3(methyl)–H 0.96 Å, 1.5U_{eq}(C)]. The hydrogen atom belonging to the oxime O1 atom was refined as a rotating group with idealized tetrahedral geometry. The molecular graphics were done with MERCURY (Version 1.4.2) [66]. Crystal data and details of the structure determination for PAM3-I are given in Table S1. Crystallographic data for PAM3-I have been deposited with the CCDC as Supplementary Data, number CCDC 2525701.

3.6. Electronic Absorption Spectral Studies

3.6.1. Determination of Ionization Constants of *N*-Methylpyridinium Aldoximes

The UV–Vis spectra of PAM2-Cl, PAM3-I, and PAM4-I in aqueous solutions (c = 4 × 10^{-5} mol dm^{-3}) were recorded at 25 °C and ionic strength I = 0.10 mol dm^{-3} in the pH range 4–11.5 (Figures S2 and S3). Ionization constants and spectral parameters of the individual ionic forms were obtained from absorbance against pH plots by nonlinear regression, as described previously [28] (Figure S4). The absorbance values at the wavelengths of absorption maxima were fitted to the equation

$$A = \frac{A(\mathrm{PAMH^+})\,[\mathrm{H^+}] + A(\mathrm{PAM^0})\,K_a}{[\mathrm{H^+}] + K_a},$$

where $A(PAMH^+)$ and $A(PAM^0)$ denote the absorbances of the protonated and deprotonated species, respectively.

3.6.2. Kinetic Investigation of Reactions Involving Pentacyano(*N*-methylpyridinium aldoxime)ferrate(II) Complexes

The kinetic study on the formation and dissociation of $[Fe(CN)_5$(pyridinium aldoxime$)]^{(3-n)-}$ complexes was performed as it had been described formerly [25]. The formation kinetics of $[Fe(CN)_5(PAMH)]^{2-}$ complexes were investigated spectrophotometrically by monitoring the absorbance increase at λ_{max}(MLCT) at 25 °C, pH 6.0 and ionic strength I = 0.10 mol dm^{-3}. Pseudo-first-order conditions were maintained using a 30- to 130-fold molar excess of the pyridinium aldoxime ligand relative to $[Fe(CN)_5(H_2O)]^{3-}$, which was held

at 5 × 10^{-5} mol dm^{-3} in all kinetic runs. L-Ascorbic acid (c_0 = 1 × 10^{-4} mol dm^{-3}) was added to all reaction mixtures in excess relative to the aquapentacyanoferrate(II) to prevent its oxidation. The pseudo-first-order rate constants (k_{obs}) were obtained from linear least-squares fits of ln (A_∞–A_t) versus time, where A_t is the absorbance at time t and A_∞ is the final absorbance at completion of the reaction. All measurements were performed in triplicate. The second-order rate constant for the complex formation (k_f) was determined as the slope of the linear plot of k_{obs} versus ligand concentration (Figure S8).

The dissociation kinetics of $[Fe(CN)_5(PAMH_n)]^{(3-n)-}$ complexes were examined under pseudo-first-order conditions by monitoring the decrease in absorbance at λ_{max}(MLCT) upon addition of a large excess of DMSO (c = 0.25 mol dm^{-3}), used as a scavenger ligand. Quantitative formation of the complexes in the initial reaction mixtures was ensured by employing a 25-fold excess of the pyridinium aldoxime ligand to 5 × 10^{-5} mol dm^{-3} $[Fe(CN)_5(H_2O)]^{3-}$. L-Ascorbic acid (c_0 = 1 × 10^{-4} mol dm^{-3}) was added to all reaction mixtures. The pseudo-first-order dissociation rate constants (k_d) were determined from linear plots of ln A_t against time. All dissociation measurements were performed in triplicate over the pH range 4–11.5. The rate constants for the dissociation of the protonated (k_{d1}) and deprotonated (k_{d2}) ligand from the $[Fe(CN)_5$(pyridinium aldoxime)$]^{(3-n)-}$ complex, as well as the ionization constant of the coordinated ligand ($K_{a\ coord.}$), were obtained from a nonlinear least-squares fit of the dissociation rate constant pH profiles (Figure S7) according to the equation

$$k_d = \frac{k_{d1}[H^+] + k_{d2} K_{a\ coord.}}{[H^+] + K_{a\ coord.}}.$$

Activation parameters for the dissociation were determined at pH 6 from the Eyring–Polanyi equation, using linear plots of ln $[(k_d/T)/(s^{-1} K^{-1})]$ against 1/T over the temperature range 10–30 °C (Figure S9; data in Table S8).

3.7. Computational Details

All molecular geometries were optimized using the M06-2X functional. The Fe atom was described using the LanL2TZ basis set and corresponding effective core potential (ECP), while all remaining atoms (C, H, N, and O) were treated with the all-electron 6-311++G(d,p) basis set, both recommended for accurate geometries and energies involving these types of molecules [67]. This choice was prompted by its success in reproducing geometries, dipole moments, and homolytic bond energies in various metal complexes, [68] and in line with our earlier reports on similar organometallic systems [69,70]. All species were modeled in aqueous solution using the implicit Solvation Model based on Density (SMD). No explicit counterions were included; charged ligands and complexes were treated directly within the continuum solvation framework. Subsequent frequency analysis provided thermal corrections, ensuring that all reported computational data correspond to Gibbs free energies at 298.15 K and 1 atm. pK_a values were calculated using an absolute method, incorporating the gas-phase free energy of a proton, $G(H^+)$ = 6.28 kcal mol^{-1}, and its experimental aqueous-phase solvation free energy, $\Delta G_{SOLV}(H^+)$ = −265.9 kcal mol^{-1} [71], consistent with the value used by Truhlar et al. [72] in parameterizing the SMD model. This solvation energy includes a free energy contribution of −1.89 kcal mol^{-1} to account for the transition from a gas-phase pressure of 1 atm to a liquid-phase concentration of 1 mol dm^{-3}. Atomic charges were obtained through the natural bond orbital (NBO) analysis [73]. UV–Vis electronic transitions were calculated using the (SMD)/CAM-B3LYP/6-311++G(d,p) single-point calculations with the TD-DFT approach, considering the 32 lowest-energy singlet electronic excitations, in line with our earlier reports on similar systems [74,75]. All calculations were performed using the Gaussian 16 program package [76].

4. Conclusion

This comparative study elucidates the distinct physicochemical differences arising from the relative position of the oxime group in *N*-methylpyridinium aldoxime isomers. The results indicate that the quinoid character of $PAM2H^+$ and $PAM4H^+$, observed in the solid-state structures of their halide salts, is also preserved in aqueous solution. This feature reflects substantial π-electron localization within the system, resulting in similar electronic structures for the *ortho*- and *para*-isomers. In contrast, the charge distribution within the *meta*-isomer indicates an absence of these resonance effects and a high degree of π-delocalization, yielding a unique electronic fingerprint characterized by an additional HOMO→LUMO+1 π–π* transition. These structurally driven electronic perturbations correlate well with the $PAM3H^+$ lower acidity. Furthermore, the charge-distribution analysis following the deprotonation of the oxime group revealed counterintuitive trends: although ionization is expected to enhance nucleophilicity, only a minor fraction of the generated charge remains on the oxime oxygen. Consequently, zwitterions likely exhibit only a modest increase in nucleophilicity, while the coordinating oxime nitrogen becomes less nucleophilic due to reduced σ-donating capability. In aqueous solutions, the ligands form intensely colored pentacyano(*N*-methylpyridinium aldoxime)ferrate(II) complexes, coordinating exclusively through the oxime nitrogen. While complex formation rates depend on the position of the oxime group, dissociation rates are comparable across isomers and weakly pH-dependent. Overall, these pyridinium oximes act as predominant σ-donors and moderate π-acceptors, producing kinetically labile and thermodynamically moderately stable complexes. Notably, while the stability constants of $PAM3H^+$ and $PAM4H^+$ complexes are comparable, their dissociation kinetics differ. The higher dissociation rate of $PAM3H^+$ complex aligns with its blue-shifted MLCT band (~90 nm), indicating weaker π-back-bonding due to the lack of resonance stabilization in the *meta*-derivative. Conversely, $PAM2H^+$ complex mirrors the kinetic behavior of $PAM4H^+$ complex due to resonance similarities, yet its thermodynamic stability is compromised by the pronounced ligand distortion (72° rotation). This highlights a clear trade-off between electronic stabilization and steric hindrance. Finally, computational analysis consistently aligns with experimental data, providing a mechanistic explanation of the experimentally observed trends and establishes a transferable conceptual model that can be used to anticipate the behavior of structurally related pyridinium oxime derivatives.

Supplementary Materials: The following supporting information can be downloaded at: https://www.mdpi.com/article/10.3390/ijms27042015/s1.

Author Contributions: Conceptualization, D.M., I.P., B.F. and V.D.; methodology, D.M., R.V., D.M.-Č., B.F. and V.D.; software, R.V.; validation, D.M., R.V. and V.D.; formal analysis, D.M., R.V., D.M.-Č., B.F. and V.D.; investigation, D.M., I.P., R.V., D.M.-Č. and V.D.; resources, V.D.; data curation, D.M., I.P., R.V. and V.D.; writing—original draft preparation, D.M., I.P., R.V., D.M.-Č. and V.D.; writing—review and editing, D.M., I.P., R.V., B.F. and V.D.; visualization, D.M., R.V., D.M.-Č. and V.D.; supervision, B.F. and V.D.; project administration, V.D.; funding acquisition, V.D. All authors have read and agreed to the published version of the manuscript.

Funding: This research was funded by the University of Zagreb research support grant FEOKS, grant number 10106-24-1510.

Institutional Review Board Statement: Not applicable.

Informed Consent Statement: Not applicable.

Data Availability Statement: The original contributions presented in this study are included in the article/Supplementary Material. Further inquiries can be directed to the corresponding author.

Acknowledgments: R.V. thanks the Zagreb University Computing Centre (SRCE) for granting computational resources on the SUPEK supercomputer.

Conflicts of Interest: The authors declare no conflicts of interest.

References

1. Jokanović, M.; Stojiljković, M.P.; Kovač, B.; Ristić, D. Pyridinium Oximes in the Treatment of Poisoning with Organophosphorus Compounds. In *Handbook of Toxicology of Chemical Warfare Agents*, 3rd ed.; Gupta, R.C., Ed.; Academic Press: Oxford, UK, 2020; pp. 1145–1159. https://doi.org/10.1016/B978-0-12-819090-6.00068-4.
2. Costanzi, S.; Machado, J.-H.; Mitchell, M. Nerve Agents: What They Are, How They Work, How to Counter Them. *ACS Chem. Neurosci.* **2018**, *9*, 873–885. https://doi.org/10.1021/acschemneuro.8b00148.
3. Petroianu, G.A.; Missler, A.; Zuleger, K.; Thyes, C.; Ewald, V.; Maleck, W.H. Enzyme Reactivator Treatment in Organophosphate Exposure: Clinical Relevance of Thiocholinesteratic Activity of Pralidoxime. *J. Appl. Toxicol.* **2004**, *24*, 429–435. https://doi.org/10.1002/jat.995.
4. Šinko, G.; Čalić, M.; Kovarik, Z. *para*- and *ortho*-Pyridinium Aldoximes in Reaction with Acetylthiocholine. *FEBS Lett.* **2006**, *580*, 3167–3172. https://doi.org/10.1016/j.febslet.2006.04.070.
5. Foretić, B.; Damjanović, V.; Vianello, R.; Picek, I. Novel Insights into the Thioesterolytic Activity of *N*-Substituted Pyridinium-4-oximes. *Molecules* **2020**, *25*, 2385. https://doi.org/10.3390/molecules25102385.
6. Zheng, S.; Pan, J.; Wang, J.; Liu, S.; Zhou, T.; Wang, L.; Jia, H.; Chen, Z.; Peng, Q.; Guo, T. Ag(I) Pyridine–Amidoxime Complex as the Catalysis Activity Domain for the Rapid Hydrolysis of Organothiophosphate-Based Nerve Agents: Mechanistic Evaluation and Application. *ACS Appl. Mater. Interfaces* **2021**, *13*, 34428–34437. https://doi.org/10.1021/acsami.1c09003.
7. Dhuguru, J.; Zviagin, E.; Skouta, R. FDA-Approved Oximes and Their Significance in Medicinal Chemistry. *Pharmaceuticals* **2022**, *15*, 66. https://doi.org/10.3390/ph15010066.
8. Sepsova, V.; Karasova, J.Z.; Korabecny, J.; Dolezal, R.; Zemek, F.; Bennion, B.J.; Kuca, K. Oximes: Inhibitors of Human Recombinant Acetylcholinesterase. A Structure-Activity Relationship (SAR) Study. *Int. J. Mol. Sci.* **2013**, *14*, 16882–16900. https://doi.org/10.3390/ijms140816882.
9. Eyer, P. The Role of Oximes in the Management of Organophosphorus Pesticide Poisoning. *Toxicol. Rev.* **2003**, *22*, 165–190. https://doi.org/10.2165/00139709-200322030-00004.
10. Kovarik, Z.; Calić, M.; Sinko, G.; Bosak, A.; Berend, S.; Lucić Vrdoljak, A.; Radić, B. Oximes: Reactivators of Phosphorylated Acetylcholinesterase and Antidotes in Therapy Against Tabun Poisoning. *Chem. Biol. Interact.* **2008**, *175*, 173–179. https://doi.org/10.1016/j.cbi.2008.04.011.
11. Worek, F.; Thiermann, H.; Szinicz, L.; Eyer, P. Kinetic Analysis of Interactions between Human Acetylcholinesterase, Structurally Different Organophosphorus Compounds and Oximes. *Biochem. Pharmacol.* **2004**, *68*, 2237–2248. https://doi.org/10.1016/j.bcp.2004.07.038.
12. Kuča, K.; Račáková, V.; Jun, D. Structure–Activity Relationships for in Vitro Oxime Reactivation of Chlorpyrifos-Inhibited Acetylcholinesterase. *Chem. Pap.* **2007**, *61*, 256–261. https://doi.org/10.2478/s11696-007-0030-7.
13. Jun, D.; Musilova, L.; Pohanka, M.; Jung, Y.-S.; Bostik, P.; Kuca, K. Reactivation of Human Acetylcholinesterase and Butyrylcholinesterase Inhibited by Leptophos-Oxon with Different Oxime Reactivators in Vitro. *Int. J. Mol. Sci.* **2010**, *11*, 2856–2863. https://doi.org/10.3390/ijms11082856.
14. Antonijevic, B.; Stojiljkovic, M.P. Unequal Efficacy of Pyridinium Oximes in Acute Organophosphate Poisoning. *Clin. Med. Res.* **2007**, *5*, 71–82. https://doi.org/10.3121/cmr.2007.701.
15. Worek, F.; Thiermann, H.; Wille, T. Oximes in Organophosphate Poisoning: 60 Years of Hope and Despair. *Chem. Biol. Interact.* **2016**, *259*, 93–98. https://doi.org/10.1016/j.cbi.2016.04.032.
16. Lindgren, C.; Forsgren, N.; Hoster, N.; Akfur, C.; Artursson, E.; Edvinsson, L.; Svensson, R.; Worek, F.; Ekström, F.; Linusson, A. Broad-Spectrum Antidote Discovery by Untangling the Reactivation Mechanism of Nerve-Agent-Inhibited Acetylcholinesterase. *Chem. Eur. J.* **2022**, *28*, e202200678. https://doi.org/10.1002/chem.202200678.
17. Kongkaew, N.; Hengphasatporn, K.; Injongkol, Y.; Mee-udorn, P.; Shi, L.; Mahalapbutr, P.; Maitarad, P.; Harada, R.; Shigeta, Y.; Rungrotmongkol, T.; et al. Design of Electron-Donating Group Substituted 2-PAM Analogs as Antidotes for Organophosphate Insecticide Poisoning. *RSC Adv.* **2023**, *13*, 32266–32275. https://doi.org/10.1039/D3RA03087C.
18. Naweephattana, P.; Kongkaew, N.; Surawatanawong, P.; Kungwan, N.; Fang, Y.; Wolschann, P.; Maitarad, P.; Hengphasatporn, K.; Shigeta, Y.; Rungrotmongkol, T.; et al. Mechanistic Insights into Enhanced Reactivation of Organophosphate-Inhibited

Enzymes by Methyl-Substituted 2-Pralidoxime Analogs. *J. Phys. Chem. B* **2025**, *129*, 5698–5706. https://doi.org/10.1021/acs.jpcb.5c01375.

19. Franjesevic, A.J.; Sillart, S.B.; Beck, J.M.; Vyas, S.; Callam, C.S.; Hadad, C.M. Resurrection and Reactivation of Acetylcholinesterase and Butyrylcholinesterase. *Chem. Eur. J.* **2019**, *25*, 5337–5371. https://doi.org/10.1002/chem.201805075.
20. Hung, L.-W.; Sanbonmatsu, K.Y.; Williams, R.F.; Chen, J.C.-H. Acetylcholinesterase: Structure, Dynamics, and Interactions with Organophosphorus Compounds. *Protein Sci.* **2025**, *34*, e70297. https://doi.org/10.1002/pro.70297.
21. Kuca, K.; Musilek, K.; Jun, D.; Zdarova-Karasova, J.; Nepovimova, E.; Soukup, O.; Hrabinova, M.; Mikler, J.; Franca, T.C.C.; Da Cunha, E.F.F.; et al. A Newly Developed Oxime K203 Is the Most Effective Reactivator of Tabun-Inhibited Acetylcholinesterase. *BMC Pharmacol. Toxicol.* **2018**, *19*, 8. https://doi.org/10.1186/s40360-018-0196-3.
22. Amitai, G.; Plotnikov, A.; Chapman, S.; Lazar, S.; Gez, R.; Loewenthal, D.; Shurrush, K.A.; Cohen, G.; Solmesky, L.J.; Barr, H.; et al. Non-Quaternary Oximes Detoxify Nerve Agents and Reactivate Nerve Agent-Inhibited Human Butyrylcholinesterase. *Commun. Biol.* **2021**, *4*, 573. https://doi.org/10.1038/s42003-021-02061-w.
23. Bondar, D.; Smirnova, O.; Nagappa, N.M.; Heinmaa, I.; Soukup, O.; Kobrlova, T.; Opravil, J.; Hrabinova, M.; Jun, D.; Starkov, P.; et al. Nanodiamond-Mediated Delivery of Pyridinium Oxime Antidotes to Central Nervous System for Potential Treatment of Exposure to Nerve Agents. *Chem. Biol. Interact.* **2025**, *420*, 111711. https://doi.org/10.1016/j.cbi.2025.111711.
24. Carlström, D. A Crystallographic Study of *N*-Methyl-pyridine-2-aldoxime (2-PAM) Halides. *Acta Chem. Scand.* **1966**, *20*, 1240–1246. https://doi.org/10.3891/acta.chem.scand.20-1240.
25. Foretić, B.; Picek, I.; Damjanović, V.; Cvijanović, D.; Pulić, I.; Kukovec, B.-M.; Matković-Čalogović, D. Spectroscopic and Structural Insights into *N*-Substituted Pyridinium-4-aldoximes and Their Pentacyanoferrate(II) Complexes. *Polyhedron* **2013**, *52*, 733–742. https://doi.org/10.1016/j.poly.2012.07.077.
26. Castro, A.T.; Figueroa-Villar, J.D. Molecular Structure, Conformational Analysis and Charge Distribution of Pralidoxime: Ab Initio and DFT Studies. *Int. J. Quantum Chem.* **2002**, *89*, 135–146. https://doi.org/10.1002/qua.10302.
27. Vyas, S.; Hadad, C.M. Reactivation of Model Cholinesterases by Oximes and Intermediate Phosphyloximes: A Computational Study. *Chem. Biol. Interact.* **2008**, *175*, 187–191. https://doi.org/10.1016/j.cbi.2008.05.006.
28. Foretić, B.; Picek, I.; Damjanović, V.; Cvijanović, D.; Milić, D. The Structures and Stabilities of Biologically Active 1-Phenacyl- and 1-Benzoylethyl-Derivatives of the Pyridinium Cation. *J. Mol. Struct.* **2012**, *1019*, 196–205. https://doi.org/10.1016/j.molstruc.2012.03.060.
29. Foretić, B.; Picek, I.; Đilović, I.; Burger, N. Preparation, Characterization and Reactivity of 1-Benzylpyridinium-4-aldoxime chloride and 1-Phenacylpyridinium-4-aldoxime chloride and Their Complexes with the Aquapentacyanoferrate(II) Ion. *Inorg. Chim. Acta* **2010**, *363*, 1425–1434. https://doi.org/10.1016/j.ica.2010.01.041.
30. Schmidt, H.; Oglou, R.C.; Tunçer, H.O.; Ghobadi, T.G.U.; Tekir, Ş.; Sertcelik, K.N.O.; Ibrahim, A.; Döhler, L.; Özçubukçu, S.; Kupfer, S.; et al. A Heterodox Approach for Designing Iron Photosensitizers: Pentacyanoferrate(II) Complexes with Monodentate Bipyridinium/Pyrazinium-Based Acceptor Ligands. *Inorg. Chem.* **2025**, *64*, 7079–7087. https://doi.org/10.1021/acs.inorgchem.5c00412.
31. Kroth, R.; Monteiro, M.C.; Conte, J.; Argenta, D.F.; Amaral, B.R.; Szpoganicz, B.; Caon, T. Transbuccal Delivery of Metal Complexes of Isoniazid as an Alternative to Overcome Antimicrobial Resistance Problems. *Int. J. Pharm.* **2020**, *590*, 119924. https://doi.org/10.1016/j.ijpharm.2020.119924.
32. Carvalho, E.M.; de Freitas Paulo, T.; Saquet, A.S.; Abbadi, B.L.; Macchi, F.S.; Bizarro, C.V.; de Morais Campos, R.; Ferreira, T.L.A.; do Nascimento, N.R.F.; Lopes, L.G.F.; et al. Pentacyanoferrate(II) Complex of Pyridine-4- and Pyrazine-2-hydroxamic acid as Source of HNO: Investigation of Anti-Tubercular and Vasodilation Activities. *J. Biol. Inorg. Chem.* **2020**, *25*, 887–901. https://doi.org/10.1007/s00775-020-01805-z.
33. Papadakis, R. Chromotropism of Iron(II) Complexes with Non-Symmetric Heterocyclic Ligands: Polarity Sensing in Aqueous Urea Solutions. *Nanomaterials* **2025**, *15*, 598. https://doi.org/10.3390/nano15080598.
34. Macartney, D.H. Properties and Reactions of Substituted Pentacyanoferrate(II) Complexes. *Rev. Inorg. Chem.* **1988**, *9*, 101–152. https://doi.org/10.1515/REVIC.1988.9.2-3.101.
35. Baran, Y.; Ülgen, A. Kinetics and Equilibrium Constants of Some Pentacyanoferrate(II) Complexes of Nitrogen and Sulfur Containing Heterocycles. *Int. J. Chem. Kinet.* **1998**, *30*, 415–418. https://doi.org/10.1002/(SICI)1097-4601(1998)30:6<415::AID-KIN3>3.0.CO;2-V.
36. Foretić, B.; Vianello, R.; Matković-Čalogović, D.; Jadreško, D.; Picek, I**.** Supramolecular Inter-Ionic Charge-Transfer Complexes between Derivatives of Pyridinium-4-oxime Cations and Hexacyanoferrate(II) Anions. *New J. Chem.* **2018**, *42*, 16115–16126. https://doi.org/10.1039/C8NJ03066A.

37. Foretić, B.; Klaser, T.; Ovčar, J.; Lončarić, I.; Žilić, D.; Šantić, A.; Štefanić, Z.; Bjelopetrović, A.; Popović, J.; Picek, I. The Reversible Electron Transfer Within Stimuli-Responsive Hydrochromic Supramolecular Material Containing Pyridinium Oxime and Hexacyanoferrate(II) Ions. *Molecules* **2024**, *29*, 5611. https://doi.org/10.3390/molecules29235611.
38. Van Havere, W.; Lenstra, A.T.H.; Geise, H.J.; Van den Berg, G.R.; Benschop, H.P. 2-[(Hydroxyimino)methyl]-1-methylpyridinium Chloride. *Acta Crystallogr. Sect. B* **1982**, *38*, 2516–2518. https://doi.org/10.1107/S0567740882009248.
39. John, H.; Blum, M.-M. Review of UV Spectroscopic, Chromatographic, and Electrophoretic Methods for the Cholinesterase Reactivating Antidote Pralidoxime (2-PAM). *Drug Test. Anal.* **2012**, *4*, 179–193. https://doi.org/10.1002/dta.327.
40. Blanch, J.H.; Onsager, O.T. Stability of *N*-Heterocyclic Oxime Derivatives. Part I. Decomposition of *N*-Methylpyridinium 3- and 4-*O*-acetyladoxime Iodides in Aqueous Solution. *J. Chem. Soc.* **1965**, 3729–3734. https://doi.org/10.1039/JR9650003729.
41. Hampl, F.; Mazac, J.; Liska, F.; Srogl, J.; Kabrt, L.; Suchanek, M. Quaternary Heteroarenium Aldoximes as Catalysts for Cleavage of Phosphate Esters. *Collect. Czech. Chem. Commun.* **1995**, *60*, 883–893. https://doi.org/10.1135/cccc19950883.
42. Green, A.L.; Saville, B. The Reaction of Oximes with isoPropyl Methylphosphonofluoridate (Sarin). *J. Chem. Soc.* **1956**, 3887–3892. https://doi.org/10.1039/JR9560003887.
43. Ginsburg, S.; Wilson, I.B. Oximes of the Pyridine Series. *J. Am. Chem. Soc.* **1957**, *79*, 481–485. https://doi.org/10.1021/ja01559a067.
44. Mason, S.F. Tautomerism of *N*-Heteroaromatic Aldoximes. *J. Chem. Soc.* **1960**, 22–26. https://doi.org/10.1039/JR9600000022.
45. Augustinsson, K.-B.; Hasselquist, H.; Larsson, L. Pyridine-*N*-Oxide-Aldoximes: Their Synthesis, and Chemical and Biochemical Properties. *Acta Chem. Scand.* **1960**, *14*, 1253–1260. https://doi.org/10.3891/acta.chem.scand.14-1253.
46. Mohaček Grošev, V.; Foretić, B.; Gamulin, O. Vibrational Analysis of 1-Methyl-pyridinium-2-aldoxime and 1-Methyl-pyridinium-4-aldoxime Cations. *Spectrochim. Acta Part A Mol. Biomol. Spectrosc.* **2011**, *78*, 1376–1379. https://doi.org/10.1016/j.saa.2011.01.012.
47. Toma, H.E.; Batista, A.A; Gray, H.B. Pentacyanoferrate(II) Complexes of Amino Acids. *J. Am. Chem. Soc.* **1982**, *104*, 7509–7515. https://doi.org/10.1021/ja00390a020.
48. Murakami Iha, N.Y.; Toma, H.E. Synthesis and Mechanisms of Formation of Pyridinecarbonyloximes by Addition Reactions to the Nitroprusside Ion. *Inorg. Chim. Acta* **1984**, *81*, 181–186. https://doi.org/10.1016/S0020-1693(00)88756-3.
49. Toma, H.E.; Malin, J.M.; Giesbrecht, E. The Ion Pentacyano(dimethyl sulfoxide)ferrate(II). Synthesis, Characterization and Substitution Kinetics in Aqueous Solution. *Inorg. Chem.* **1973**, *12*, 2084–2089. https://doi.org/10.1021/ic50127a027.
50. Toma, H.E.; Malin, J.M. Properties and Reactivity of Some Pentacyanoferrate(II) Complexes of Aromatic Nitrogen Heterocycles. *Inorg. Chem.* **1973**, *12*, 1039–1045. https://doi.org/10.1021/ic50123a013.
51. Moreno, N.G.d.V.; Katz, N.E.; Olabe, J.A.; Aymonino, P.J. 3-and 4-Cyanopyridine Complexes of Pentacyanoferrate(II) and Pentacyanocobaltate(III). *Inorg. Chim. Acta* **1979**, *35*, 183–188. https://doi.org/10.1016/S0020-1693(00)93437-6.
52. Foucher, D.A.; Macartney, D.H.; Warrack, L.J.; Wilson, J.P. Kinetics and Mechanism of Ligand Substitution Reactions of Pentacyanoferrate(II) Complexes with Bridging *N*-Heterocyclic Dications in Aqueous Media. *Inorg. Chem.* **1993**, *32*, 3425–3432. https://doi.org/10.1021/ic00068a010.
53. Ekström, F.; Pang, Y.-P.; Boman, M.; Artursson, E.; Akfur, C.; Börjegren, S. Crystal Structures of Acetylcholinesterase in Complex with HI-6, Ortho-7 and Obidoxime: Structural Basis for Differences in the Ability to Reactivate Tabun Conjugates. *Biochem. Pharmacol.* **2006**, *72*, 597–607. https://doi.org/10.1016/j.bcp.2006.05.027.
54. Wanat, A.; van Eldik, R.; Stochel, G. Kinetics and Mechanism of the Reduction of Pentacyanonitroferrate(III) by L-Ascorbic Acid in Acidic Aqueous Solution. *J. Chem. Soc. Dalton Trans.* **1998**, 2497–2501. https://doi.org/10.1039/A802821D.
55. James, A.D.; Murray, R.S. Kinetics of Formation and Bridge Cleavage of Binuclear Complexes derived from the Pentacyanoferrate(II and III) Ions in Aqueous Solution. *J. Chem. Soc. Dalton Trans.* **1977**, 326–329. https://doi.org/10.1039/DT9770000326.
56. Lin, L.-M.; Lien, M.-H.; Yeh, A. Kinetic Studies of the Reactions of Pentacyanoferrate(III) Complexes with L-Ascorbic Acid. *Int. J. Chem. Kinet.* **2005**, *37*, 126–133. https://doi.org/10.1002/kin.20052.
57. Mongay, C.; Cerda, V. A Britton–Robinson Buffer of Known Ionic Strength. *Ann. Chim.* **1974**, *64*, 409–412.
58. Waysbort, D.; Balderman, D.; Amitai, G. Carbon-13 NMR Characterization of the Bispyridinium Oximes, Toxogonin, HS-3, HS-6 and HI-6. *Org. Magn. Reson.* **1981**, *16*, 7–10. https://doi.org/10.1002/mrc.1270160103.
59. Musílek, K.; Lipka, L.; Račáková, V.; Kuča, K.; Jun, D.; Dohnal, V.; Doležal, M. New Methods in Synthesis of Acetylcholinesterase Reactivators and Evaluation of Their Potency to Reactivate Cyclosarin-Inhibited AChE. *Chem. Pap.* **2006**, *60*, 48–51. https://doi.org/10.2478/s11696-006-0008-x.
60. Marusak, R.A.; Doan, K.; Cummings, S.D. *Integrated Approach to Coordination Chemistry: An Inorganic Laboratory Guide*; Wiley: Hoboken, NJ, USA, 2007; p. 89.

61. Ulusoy Ghobadi, T.G.; Akhuseyin Yildiz, E.; Buyuktemiz, M.; Sadigh Akbari, S.; Topkaya, D.; İsci, Ü.; Dede, Y.; Yaglioglu, H.G.; Karadas, F. A Noble-Metal-Free Heterogeneous Photosensitizer-Relay Catalyst Triad that Catalyzes Water Oxidation under Visible Light. *Angew. Chem. Int. Ed.* **2018**, *57*, 17173–17177. https://doi.org/10.1002/anie.201811570.
62. *CrysAlisPro Software System*, version 171.37.33; Agilent Technologies UK, Ltd.: Oxford, UK, 2012.
63. Dolomanov, O.V.; Bourhis, L.J.; Gildea, R.J.; Howard, J.A.K.; Puschmann, H. OLEX2: A Complete Structure Solution, Refinement and Analysis Program. *J. Appl. Cryst.* **2009**, *42*, 339–341. https://doi.org/10.1107/S0021889808042726.
64. Sheldrick, G.M. A Short History of SHELX. *Acta Cryst. A* **2008**, *64*, 112–122. https://doi.org/10.1107/S0108767307043930.
65. Sheldrick, G.M. Crystal structure refinement with SHELXL. *Acta Cryst. C* **2015**, *71*, 3–8. https://doi.org/10.1107/S2053229614024218.
66. Macrae, C.F.; Bruno, I.J.; Chisholm, J.A.; Edgington, P.R.; McCabe, P.; Pidcock, E.; Rodriguez-Monge, L.; Taylor, R.; van de Streek, J.; Wood, P.A. Mercury CSD 2.0—New Features for the Visualization and Investigation of Crystal Structures. *J. Appl. Crys.* **2008**, *41*, 466–470. https://doi.org/10.1107/S0021889807067908.
67. Bursch, M.; Mewes, J.; Hansen, A.; Grimme, S. Best-Practice DFT Protocols for Basic Molecular Computational Chemistry. *Angew. Chem. Int. Ed.* **2022**, *61*, e202205735. https://doi.org/10.1002/anie.202205735.
68. Cramer, C.J.; Truhlar, D.G. Density Functional Theory for Transition Metals and Transition Metal Chemistry. *Phys. Chem. Chem. Phys.* **2009**, *11*, 10757–10816. https://doi.org/10.1039/B907148B.
69. Jakopec, S.; Pantalon Juraj, N.; Jadreško, D.; Vianello, R.; Brozovic, A.; Tadić, V.; Milić, L.; Perić, B.; Raić-Malić, S.; Kirin, S.I. Late Transition Metal Complexes of Ferrocene-containing Nitrogen Ligands: Coordination Chemistry, Electron Transfer Properties, and Tumor Cell Viability. *Appl. Organomet. Chem.* **2024**, *38*, e7415. https://doi.org/10.1002/aoc.7415.
70. Bakija, M.; Perić, B.; Rinkovec, T.; Sanders, E.; Kokan, Z.; Štefanić, Z.; Vianello, R.; Kirin, S.I. Induction of Helical Chirality in Tetrahedral Transition Metal Complexes with Non-bridging Monodentate Oxazolines. *Dalton Trans.* **2025**, *54*, 17083–17101. https://doi.org/10.1039/d5dt02399h.
71. Tissandier, M.D.; Cowen, K.A.; Feng, W.Y.; Gundlach, E.; Cohen, M.H.; Earhart, A.D.; Coe, J.V.; Tuttle, T.R. The Proton's Absolute Aqueous Enthalpy and Gibbs Free Energy of Solvation from Cluster-Ion Solvation Data. *J. Phys. Chem. A* **1998**, *102*, 7787–7794. https://doi.org/10.1021/jp982638r.
72. Marenich, A.V.; Cramer, C.J.; Truhlar, D.G. Universal Solvation Model Based on Solute Electron Density and on a Continuum Model of the Solvent Defined by the Bulk Dielectric Constant and Atomic Surface Tensions. *J. Phys. Chem. B* **2009**, *113*, 6378–6396. https://doi.org/10.1021/jp810292n.
73. Foster, J.P.; Weinhold, F. Natural Hybrid Orbitals. *J. Am. Chem. Soc.* **1980**, *102*, 7211–7218. https://doi.org/10.1021/ja00544a007.
74. Beč, A.; Vianello, R.; Hranjec, M. Synthesis and Spectroscopic Characterization of Multifunctional D-π-A Benzimidazole Derivatives as Potential pH Sensors. *J. Mol. Liq.* **2023**, *386*, 122493. https://doi.org/10.1016/j.molliq.2023.122493.
75. Galić, M.; Čikoš, A.; Persoons, L.; Daelemans, D.; Vrandečić, K.; Karnaš, M.; Hranjec, M.; Vianello, R. Benzoxazole Iminocoumarins as Multifunctional Heterocycles with Optical pH-Sensing and Biological Properties: Experimental, Spectroscopic and Computational Analysis. *Chemosensors* **2026**, *14*, 15. https://doi.org/10.3390/chemosensors14010015.
76. Frisch, M.J.; Trucks, G.W.; Schlegel, H.B.; Scuseria, G.E.; Robb, M.A.; Cheeseman, J.R.; Scalmani, G.; Barone, V.; Petersson, G.A.; Nakatsuji, H.; et al. *Gaussian 16, Revision C.01*; Fox Gaussian, Inc.: Wallingford, CT, USA, 2016.